A Method for Modeling the Aero-Propulsive Coupling Characteristics of BLI Aircraft in Conceptual Design

Jai Ahuja* and Dimitri N. Mavris [†]

Aerospace Systems Design Laboratory, School of Aerospace Engineering,
Georgia Institute of Technology, Atlanta, GA, 30332, USA

The impacts of boundary layer ingestion (BLI) on vehicle performance can be modeled using either a decoupled or a coupled approach. Several studies in literature have adopted the former, while some have shown differences between the two approaches for the performance analysis and design refinement of a sized aircraft. This study quantifies the consequences of ignoring aero-propulsive coupling at the aircraft sizing stage of conceptual design. To do so, a parametric and coupled aero-propulsive design methodology is used that leverages surrogate modeling to minimize the computational burden of CFD in generating estimates of the BLI performance impacts. The method is applied to the design and analysis of two BLI concepts with engine locations similar to that on the D8 and the NOVA-BLI.

I. Nomenclature

Important Acronyms

AR	Aspect ratio
BLI	Boundary layer ingestion
EDS	Environmental Design Space
FPR	Fan pressure ratio
HPCPR	High pressure compressor pressure ratio
LDGFL	Landing field length
LPCPR	Low pressure compressor pressure ratio
MFE	Model fit error
MRE	Model representation error
OPR	Overall pressure ratio
SWETF	Fuselage wetted area (or multiplier)
SWETN	Nacelle wetted area (or multiplier)
TOFL	Takeoff field length
TOGW	Takeoff gross weight
WSR	Wing loading

Symbols

$C_{P_{K_{in}}}$	Non dimensional $P_{K_{in}}$
d	Diameter
D'	Non-BLI aircraft drag
F'_N	Gross thrust minus freestream ram drag
h	Altitude
$\dot{m}$	Mass flow rate
M	Mach number
P_{ex}	Excess power required
$P_{K_{in}}$	Ingested mechanical energy defect
p	Static pressure
p_t	Total pressure

q	Dynamic pressure
$\mathcal{R}_i$	i^{th} residual equation
S	Wing planform area
$\bar{S}$	Wing planform area initial guess
S_{ref}	Reference area
SPW_{c_2}	Specific corrected flow at fan face
$V; \mathbf{V}$	Flow velocity magnitude; vector
$\mathbf{x}; \mathbf{x}_S$	Vector of design variables; shared variables
$\mathbf{y}; \mathbf{y}^t$	Vector of coupling variables; target variables

Greek

α	Angle of attack
β	Symbol representing BLI effects
Δ	Change in the value of a given quantity
η_{PR}	Pressure recovery
λ	Taper ratio
$\Lambda_{c/4}$	Quarter chord sweep angle
Λ_{LE}	Leading edge sweep angle
ρ	Density
ϕ	Inlet ramp angle
Φ_{surf}	Dissipation in aircraft surface boundary layer
Φ_{wake}	Dissipation in aircraft wake

Conventions

$(\cdot)'$	Non-BLI quantities
$(\cdot)_A$	Quantities related to the aerodynamics discipline
$(\cdot)_B$	Quantities related to the BLI effects model
$(\cdot)_P$	Quantities related to the propulsion discipline
$(\cdot)_\infty$	Freestream quantities

---

*PhD Candidate, Aerospace Systems Design Laboratory, Georgia Institute of Technology, AIAA Student Member

[†]S.P. Langley Distinguished Regents Professor, Georgia Institute of Technology, AIAA Fellow

II. Introduction and Background

Given the impact of fuel prices on airline operating costs, it should be no surprise that reduced fuel burn is one of the primary design drivers for each new generation of aircraft. Reductions in block fuel burn, even as small as 0.25%, can have a substantial fleet level impact. Entities like National Aeronautics and Space Administration in the United States, and the Advisory Council for Aeronautics Research in Europe, are spearheading research efforts into concepts and technologies for improved fuel efficiency [1, 2]. One promising set of concepts are Boundary Layer Ingesting (BLI) aircraft. As shown by Betz [3], the low velocity inflow for BLI propulsors reduces the power required to produce a given net momentum flux, which directly translates to fuel burn savings. There are several entities all over the world actively involved in BLI research, with a number of ideas put forward as a potential successors for the current tube and wing aircraft. These include concepts such as the N3-X Turboelectric Distributed Propulsion (TeDP) Blended Wing Body (BWB) [4, 5], STARC-ABL [6], D8 Double Bubble [7–9], and the Onera NOVA-BLI [10] to name a few. Concepts like these exhibit stronger interactions between the airframe aerodynamics and propulsion system, relative to conventional designs with podded engines, owing to the propulsor-airframe integration. What are the consequences then of ignoring this aero-propulsive coupling resulting from BLI on vehicle sizing, engine cycle design, and vehicle performance?

To answer this question, literature on the BWB, D8, STARC-ABL and NOVA-BLI concepts was reviewed, with a focus on how the aerodynamics and/or propulsion disciplines were treated in a given study. These studies are summarized in Fig. 1, tagged by concept and the lead author last name. These studies are categorized by design focus, model fidelity level, and whether the BLI aero-propulsive interactions are captured. Salient aspects of each reviewed study are concisely presented in chapter 2 of [11] for the interested reader. There are several different approaches that researchers have adopted to incorporate BLI effects in conceptual design of the airframe and engines. These approaches can be largely classified into two categories: decoupled and coupled, based on the degree of aero-propulsive interactions captured in the methodology.
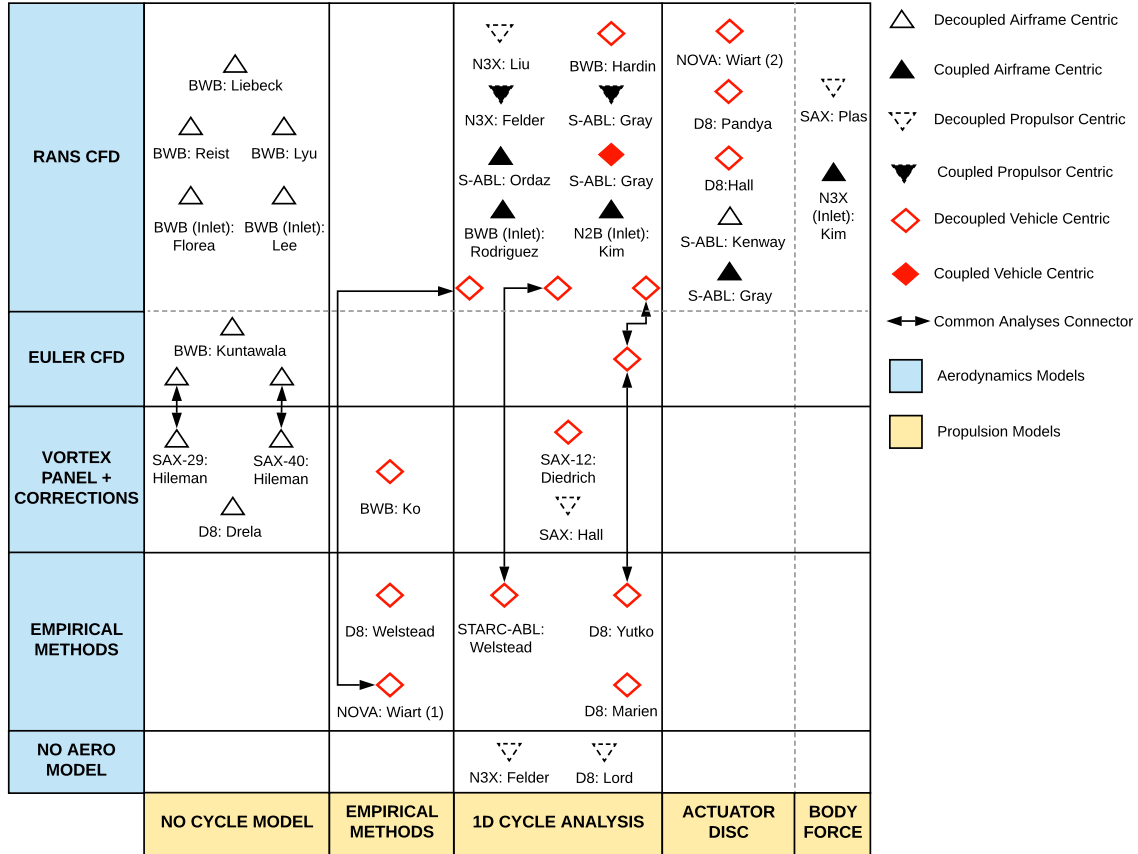

Fig. 1   Summary of reviewed literature on BLI concepts

A significant number of these studies decouple the airframe and propulsion system design and/or analysis. In other words, the aero-propulsive interactions are ignored. Coupled approaches on the other hand account for these interactions through an iterative information exchange between the aerodynamics and propulsion disciplines until a converged solution is obtained. Decoupled approaches are particularly useful when there is limited design knowledge regarding the airframe and/or the propulsor, as is usually the case in conceptual design. Conceptual proposals for the BWB [12–14], D8, STARC-ABL, and NOVA-BLI all treated the BLI problem in a decoupled fashion. Decoupled approaches are particularly amenable at this stage since, as Hendricks [15] notes, decoupled approaches do not need an integrated design environment which coordinates the execution of and the exchange of information between the aerodynamics and propulsion analysis codes. This enables a "traditional division of modeling"[15], allowing researchers to focus on their areas of expertise and use any fidelity level for modeling their disciplines, without having to incur the computational expense of ensuring compatibility with other disciplinary tools. Rapid design space exploration is thus possible early in the design stage enabling growth of design knowledge. The SAX-29 and SAX-40 concept design methodologies [16–19] are prime examples of this strategy. Decoupled approaches also facilitate development of new methodologies for design refinement by restricting the modeling scope, such as the BWB airframe optimization approaches by Kuntawala [20], Reist [21], and Lyu [22]. These methodologies can then later be embedded in coupled analyses.

However, despite the advantages of a decoupled approach, studies have shown limitations of this strategy for highly integrated concepts like BLI. Coupled analyses in literature, such as Felder's work with the N3X engine [5], Gray's [23, 24] and Ordaz's [25] analyses of the STARC-ABL concept have shown the significance of these interactions. Decoupled approaches fail to capture the interdependency between aerodynamics and propulsion, and the results are inconsistent between the two disciplines. The vehicle sized using a decoupled approach is dependent on the validity of the assumptions used for modeling the BLI impact, imparting an additional degree of uncertainty in the performance of the proposed concept. Additionally, maximizing fuel burn benefits for BLI concepts requires propulsion-airframe integration efforts that maximize favorable and minimize detrimental interactions between the airframe and propulsor. Decoupled approaches cannot be used to optimize the integrated vehicle since they do not capture this interaction. The impacts of BLI may be mis-estimated from a decoupled approach. Consequently, there is a risk that the sized vehicle will not be satisfactory or even feasible. Thus, it can be claimed that a coupled methodology for aero-propulsive design and analysis is the most appropriate way for BLI concepts.

In conceptual design, when design knowledge is limited, design space exploration is essential. Parametric variations of key vehicle features like wing area, aspect ratio, sweep, etc., facilitate this process. A parametric approach coupled to computationally inexpensive analyses enable efficient evaluation of thousands of designs. For BLI concepts, there is a need to capture the aero-propulsive coupling in this parametric design environment. However, the coupled approaches presented in literature such as those by Rodriguez [26], Gray [23, 24, 27], Ordaz [25], and Kim [28, 29] are better suited to post conceptual design stages where the vehicle has already been sized, and it is then necessary to refine the contours of the vehicle outer mold line to minimize adverse flow features like shocks or separation that are inimical to performance. Additionally, the coupled analyses reviewed are only conducted at one flight condition. The computational expense of reaching interdisciplinary compatibility, using high fidelity analyses, at each point in the flight envelope is another major limitation of these approaches. As a result, this process is unsuitable at the conceptual design stage where multiple flight conditions at key points in the mission profile need to be considered. Felder's approach [5] for modeling the boundary layer impacts on the propulsor using fixed CFD profiles, but varying the capture height, and accounting for multiple flight conditions, is one way the aero-propulsive coupling can be captured in conceptual design of BLI propulsors. However, this approach is not fully coupled given that the profile shapes are assumed to remain the same throughout the flight envelope, and for varying propulsor sizes, the latter shown by Gray to be invalid. Additionally, for vehicle centric design studies where the airframe size is also varying, the assumption of fixed boundary layer profiles and properties is no longer appropriate.

There is thus a gap in the literature. A parametric and coupled aero-propulsive design and analysis methodology that is appropriate for conceptual design BLI vehicle sizing and corresponding trade studies is needed to quantify the significance of the aero-propulsive interactions on aircraft design and performance. This effort entails i) defining and isolating the impacts of BLI on vehicle performance (BLI effects) ii) quantifying the sensitivity of these BLI effects to changes in airframe and propulsor design/operation iii) formulating correlations capturing these sensitivities and iv) integrating these expressions in a vehicle sizing environment, while leveraging best practices from existing approaches in literature. Section III describes the proposed BLI concept design methodology and introduces the experiments. Sections IV to VI describe the implementation of the methodology on the design and analysis of two tube and wing BLI configurations similar to the D8 and NOVA-BLI. Finally, section VII summarizes key takeaways and provides recommendations for future work.

III. Methodology

A. BLI Performance Impacts (BLI Effects)

To capture the aero-propulsive interactions due to BLI, one must first define a way to model the BLI performance impacts. The idea here is to treat BLI like a technology and define an appropriate set of responses that can be applied to a non-BLI configuration to determine how this this design will perform when BLI is now considered. Changes to airframe and propulsor design variables for conventional aircraft with podded engines are captured through changes in drag and thrust respectively. However, this decomposition is ambiguous for BLI concepts. Drela's power balance approach [30] is one solution. This formulation bookkeeps performance as power sources and power sinks, instead of the ill-defined thrust and drag. However, most existing engine and airframe codes still rely on thrust-drag, so a mapping between power balance and thrust-drag is needed that is unambiguous and correctly captures the BLI related physics. Recognizing that power balance is valid for both BLI and non-BLI, this approach must be equivalent in some manner to the thrust-drag bookkeeping for non-BLI aircraft. With some simple and justifiable assumptions, and based on the work by Hall [31, 32] and Drela [30], this mapping was derived in a previous paper by the author titled *Sensitivity of Boundary Layer Ingestion Effects to Tube and Wing Airframe Design Features* [33]. Moving from the BLI form of the power balance to the non-BLI version results in the identification of certain terms that are non-zero for the former, but zero for the latter. These additional terms can be called the BLI effects as they capture changes in the propulsive power requirements due to the engine ingesting the boundary layer. Thus, one can use conventional thrust-drag for sizing a non-BLI vehicle, and then account for the impacts of BLI using the power balance terminology, as shown below:

$$F_N' V_\infty = D' V_\infty + P_{\text{ex}} - \underbrace{\left(P_{K_{\text{in}}} + \Delta\Phi_{\text{wake}} + \Delta\Phi_{\text{surf}} \right)}_{\beta} \tag{1}$$

In Eq. (1), F_N' is the gross thrust minus the freestream ram drag, D' is the drag of the un-powered airframe, P_{ex} represents the excess power requirement, and β represents the BLI effects. Thus, Eq. (1) basically states that the power produced by the propulsor must balance the power required by the aircraft, the excess power requirements, and any propulsive power changes due to BLI. The reader is encouraged to refer to the work in [33] and cited papers by Drela and Hall for details on the BLI effects and the power balance method. A general description of the BLI effects and comments on the implementation strategy for this study are presented below. Fig. 2 summarizes this strategy.

1. $P_{K_{in}}$

This term captures the ingested mechanical energy defect rate and is one of the major contributors to a reduction in propulsive power. This quantity is defined by the following equation:

$$P_{K_{\text{in}}} = \iint -\left[(p - p_\infty) + \frac{1}{2}\rho \left(V^2 - V_\infty^2 \right) \right] \mathbf{V} \cdot \hat{\mathbf{n}} dA \tag{2}$$

This surface integral can be evaluated on a disc at the inlet highlight plane (as done by Hall [32]), or at the fan-face. The highlight plane ignores contributions from the inlet, which is justifiable for early conceptual design since the inlet geometry is still ill-defined. However, [34] shows a non-negligible contribution from the inlet to $P_{K_{\text{in}}}$, which is why the fan-face annulus is chosen as the integration plane in this study.

2. $\Delta\Phi_{wake}$

Captures the change in power dissipation in the airframe wake due to partial wake ingestion by the propulsor. Hall proposes two methods for estimating the change in wake dissipation. The first approach discussed in [31] is as follows:

$$\Delta\Phi_{\text{wake}} = \frac{\mathcal{K}_{\text{in}}}{\Phi'_{\text{surf}}} \Phi'_{\text{wake}} \tag{3}$$

where $\mathcal{K}_{\text{in}}$ is the ingested kinetic energy defect, as defined in standard boundary layer theory. In this approach, only the change in fuselage wake dissipation is calculated. The wing wake, comprising of shed vortices, is not included. This approach also requires estimating the terms Φ'_{surf} and Φ'_{wake} for a non-BLI configuration, which are challenging to calculate. For example, accurate estimation of Φ'_{wake} requires wake mesh refinement in CFD, which increases computational requirements, making it somewhat impractical for parametric studies requiring multiple solutions.

The second method suggested in [32] approximates the change in overall airframe wake dissipation as the reduction in amount of mechanical flow energy being deposited off the airframe, calculated using the equation below

$$\Delta \Phi_{\text{wake}} \approx \iint \left[\frac{1}{2} \rho |\mathbf{V} - \mathbf{V}_\infty|^2 \mathbf{V} \cdot \hat{\mathbf{n}} + (p - p_\infty)(\mathbf{V} - \mathbf{V}_\infty) \cdot \hat{\mathbf{n}} \right] dA_{PO} \tag{4}$$

Unlike the first method, this approach accounts for the pressure defect work rate and potential contributions from wing vortex wake ingestion, making it the preferred method for this study. In addition, the single equation formulation simplifies the calculation process. It is important to highlight that $\Delta \Phi_{\text{wake}}$ is estimated from an un-powered configuration. Integrating Eq. (4) at the propulsor outlet plane (A_{PO}) to calculate $\Delta \Phi_{\text{wake}}$ implies the following reasoning: by placing a propulsor at that location, these perturbations in the flow are ingested and thus will not dissipate in the airframe wake. With a powered engine jet, this reasoning is not valid given that perturbations in the flow arise primarily from the jet, and not from the ingested wake. Thus, an un-powered configuration needs to be defined to calculate $\Delta \Phi_{\text{wake}}$.

This un-powered configuration is the same as the BLI aircraft, with two possible ways for dealing with the engine. The first way, as done by Hall, uses a through-flow nacelle. An integration area is defined at the nozzle exit plane on which Eq. (4) is calculated. The alternative is to eliminate the through-flow nacelle geometry altogether and just leave the appropriately sized integration area on which $\Delta \Phi_{\text{wake}}$ can be evaluated. The latter approach has two advantages. First, the effect of nacelle diameter on $\Delta \Phi_{\text{wake}}$ can be captured quite easily by changing the radius of the integration area within a CFD run, without having to run additional cases. Second, based on test cases with an axisymmetric fuselage geometry and tail-cone propulsor, through-flow nacelles may produce separation bubbles in regions where such flow would not exist if a powered nacelle was present, or if no nacelle was modeled. This kind of flow skews the results. Removing the through-flow nacelle geometry ensures that the airframe and flight conditions are the primary drivers behind the solution, and not artificial propulsion integration effects due to a semi-unrealistic engine model.

3. $\Delta \Phi_{surf}$

Captures the change in power dissipation in the boundary layer over the airframe surface. The change in surface dissipation can be modeled by the change in wetted area going from the podded to the BLI configuration. Elimination of the pylons and partial embedding of the engines in the airframe, for example, contribute to reductions in wetted area. However, addition of a third nacelle, like in the STARC-ABL, contributes to an increase in surface dissipation

4. η_{PR}

Though not an explicit part of Eq. (1), pressure recovery affects the fuel flow required by the propulsor to produce a given F'_N. Pressure recovery and $P_{K_{\text{in}}}$ must be calculated at the same location. Otherwise, there is an inconsistency in bookkeeping losses and performance benefits. If $P_{K_{\text{in}}}$ is evaluated at the inlet highlight, pressure recovery is defined as p_{t_1}/p_{t_∞} and thus only captures total pressure losses in the boundary layer over the airframe surface. If inlet contributions are to be accounted for, as done in this study, $\eta_{PR} = p_{t_2}/p_{t_\infty}$
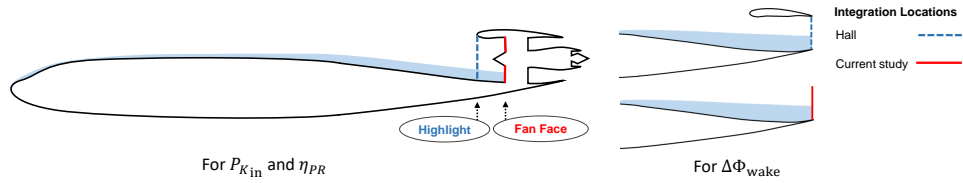
Fig. 2   Comparison of where power balance integrals are evaluated

B. Overview of Method

The main idea is to develop a BLI conceptual design methodology similar to the approach adopted for sizing conventional vehicles with non-BLI engines, but enhance that method by modeling elements that are unique to BLI concepts. There is a need for a parametric methodology, that captures the aero-propulsive interactions at the conceptual design level. As such, there is a requirement for balancing the use of high fidelity analyses to capture the BLI impacts on performance, while minimizing the overall design and analysis time by leveraging lower fidelity codes for other aspects of the vehicle sizing process, as also done in several other studies in the literature. The proposed method uses

Fig. 3 Coupled Aero-Propulsive BLI Aircraft Conceptual Design

CFD to calculate the BLI effects as a function of key airframe design parameters, propulsor design and operation, and flight conditions. Surrogate models of these BLI effects are formulated. These semi-empirical performance corrections are then integrated with low-fidelity conceptual design aircraft sizing and engine cycle analysis tools. The flowchart in Fig. 3 summarizes the proposed BLI concept design methodology. Borrowing extended design structure matrix (XDSM) [35] style elements, process flows are shown with black arrows and also imply data flows. Data flows are shown with gray lines and are highlighted in situations where there is no explicit process flow, but there is a transfer information between two processes. The overall methodology is broken down into three distinct phases: i) Pre-Vehicle Sizing ii) Vehicle Sizing iii) Vehicle Optimization. These stages are described in the following sub-sections.

C. Pre-Vehicle Sizing Stage

This is the first stage in the BLI aircraft design process. It starts with a requirements definition, where the functional and performance requirements for the aircraft are defined, and any constraints are identified. The aircraft design mission profile is also specified. At this point, a conventional (non-BLI) baseline airframe design can be defined, along with the engine architecture, and initial cycle design variables. The idea is to take a reasonable non-BLI aircraft as a starting point, and then morph it into the final BLI vehicle by accounting for the BLI effects, the aero-propulsive coupling, and the resulting changes to the airframe and engine design as a result of BLI. For example, a notional 737-8 can be a reasonable baseline on which the BLI-equivalent version (similar to the D8 and NOVA-BLI concepts) can be developed.

In parallel, sensitivity studies to assess the most significant airframe and propulsor variables impacting the BLI effects are conducted. Sensitivity of the BLI effects to the airframe design has been investigated previously [33]. With regards to the propulsor impacts on the BLI effects, these studies are described in a companion paper [34]. The sensitivity studies filter the overall design space to establish the set of variables that will feature as inputs to the surrogates of the BLI effects. Reasonable bounds are imposed on these variables to capture expected variations that occur as part of the vehicle sizing, design space exploration, and optimization routines. The baseline non-BLI aircraft developed previously serves as a reasonable initial point around which the extents of the design space can be defined.

Once the input space and flight conditions are known, a design space sampling strategy must be formulated. The number of samples is determined by the desire to maximize prediction accuracy of the surrogate model, accounting for the dimensionality of the input space, the number of CFD function calls that can be afforded, and the aircraft design

objectives. If global accuracy of the surrogates is desired, then Design of Experiments (DoE) techniques such as the widely used Latin Hypercube Sampling (LHS) [36] are appropriate. Constraints on the input variables can be imposed to avoid sampling in infeasible design regions. An example of such a constraint would be one relating the minimum and maximum permissible Mach number of the aircraft as a function of altitude. Such a constraint can be formulated by looking at a typical flight envelope. If the design space is not cubical as a result of the constraints, then computer generated custom space filling designs are needed. Traditional DoEs are inappropriate for such irregular design spaces.

If however the input space dimensionality is too large to sample adequately given computational cost constraints, then dimensionality reduction techniques can be considered. Alternatively, a smaller DoE can be used in conjunction with an adaptive sampling approach. This process allows one to obtain local accuracy (rather than global accuracy over the entire design space) in regions where maximum improvement in a metric like fuel burn is expected. The need for such approaches is ultimately determined by the results of the BLI effects sensitivity studies, and the variables of interest for the aircraft designer.

Once the sample points are known, it is merely a question of running CFD for each design sample, tracking the BLI effects, and then generating semi-empirical correlations of these responses. These models can be simple polynomial response surface equations (RSEs) [37], or something more advanced like Kriging [38] can be used. The latter technique also provides estimates for prediction uncertainty, useful when paired with an adaptive sampling strategy [39, 40]. Non-linear models such as Artificial Neural Networks (ANN) have also been used in aircraft design and optimization [41, 42], when standard linear regression models are inadequate. The methodology treats the surrogate models as a black box, so barring implementation challenges, any of the above approaches can be used.

D. Vehicle Sizing Loop

Once the BLI effects surrogates are obtained, it is possible to proceed with the vehicle sizing stage. This stage can be broken down into four sub-stages as follows: i) Engine on-design analysis ii) Engine off-design analysis iii) Engine weight and flow path analysis iv) Airframe sizing and mission analysis. Engine on-design begins by providing the propulsion model with estimates for the non-BLI baseline vehicle drag (thrust required), D', and the flight conditions at each of the n engine sizing points. The thrust requirements at this stage are merely initial guesses, which will be updated over the course of the sizing process. The initial cycle design is also known from the previous stage. A subset of the airframe design parameters from the baseline are also provided for the BLI effects surrogates. The engine is sized using the Multi-Design Point (MDP) approach [43, 44]. Within this sub-stage, multiple calls are made to the BLI effects surrogates for $P_{K_{in}}$, $\Delta\Phi_{wake}$, and η_{PR} to correct engine performance as a function of the changing engine size and operation. These surrogates are embedded within the engine analysis code, rather than as a separate external process. Thus, gray lines are used to depict data connections between the engine stages and the BLI effects surrogates in Fig. 3.

Once the engine has been sized, off-design analysis can then generate an engine deck. Again, for each point in this deck, engine performance is corrected by the BLI effects surrogates. Note that the fan size is fixed at this sub-stage. The sized engine weights and dimensions can then be estimated and values for the overall engine weight, max nacelle diameter, and nacelle length are also obtained. These results, along with the engine deck, are used in the airframe sizing process. In addition, the BLI effects surrogates also provide estimates for changes in the fuselage and nacelle wetted areas, compared to the non-BLI baseline, as a result of going to a partially embedded nacelle for the BLI configuration. These wetted area corrections are used to modify D', calculated by the airframe sizing code, thereby accounting for $\Delta\Phi_{surf}$ effects on performance.

Based on the requirements definition, airframe design parameters, and engine design and performance, the aircraft is sized and run through the specified mission. The airframe sizing code determines whether the engine performance is adequate for the sized airframe, and if not, calculates a scaling factor that updates the thrust requirements at the sizing points. Additionally, for aircraft sized using a fixed wing loading, the wing planform area is also scaled based on the final aircraft TOGW. The engine-aircraft design loop is said to converge when the following residuals defining the MDA problem are satisfied

$$\mathcal{R}_1^{(i)} = F_N' V_\infty^{(i)} - D' V_\infty^{(i)} - P_{ex}^{(i)} + \left(P_{K_{in}} + \Delta\Phi_{wake} + \Delta\Phi_{surf}\right)^{(i)} \le \epsilon \tag{5a}$$

$$\mathcal{R}_2 = S - \bar{S} \le \epsilon \tag{5b}$$

$$\forall i \in \{1, ..., n\}$$

In Eq. (5), ϵ is a user defined threshold value. The residual $\mathcal{R}_1$ is defined for each engine sizing point i. In $\mathcal{R}_2$, $\bar{S}$ is the guessed wing planform area provided to the BLI effects surrogate model at the start of the iteration and S is the

value obtained from the airframe sizing code based on the calculated TOGW and the user specified wing loading. If convergence is not achieved at a given iteration, the updated planform area and propulsor power requirements are passed back to the engine MDP sizing and this Fixed Point Iteration (FPI) repeats till convergence.

E. Vehicle Optimization Loop

Given that the BLI aircraft is developed from a non-BLI starting point, it is possible that the initial engine cycle and/or airframe design parameters are not optimal. Therefore, the vehicle sizing MDA loop can be repeated multiple times for a sweep of cycle design parameters and key airframe geometry variables in a design space exploration study. Optionally, the MDA problem can be extended to include simultaneous optimization of the cycle and airframe to minimize some system level metric like fuel burn for example. In this optimization, each function call corresponds to one vehicle sizing FPI, and is thus a Multidisciplinary Feasible (MDF) MDAO architecture [45]. MDF is a monolithic architecture that links an optimization algorithm to an MDA solver. As a result, the optimizer sees a disciplinary consistent solution for every function call. If the line search in the optimization algorithm has converged, based on algorithm dependent convergence criteria, the constraints imposed on the problem can be evaluated. If the chosen point satisfies the constraints, and the optimization convergence criteria, then the optimum solution is obtained. If not, the cycle and airframe design variables need to be perturbed and process repeats as shown in Fig. 3.

Since the MDF architecture treats the MDA problem as a single black-box function, it makes no difference to the optimizer whether the function values and gradients are being provided directly by the disciplinary analysis codes, or by surrogate models of the converged responses of interest. Factors like design space dimensionality, significance of interdisciplinary coupling, and ease of interfacing several analysis codes determine the appropriate course of action. There are two potential advantages to the surrogate approach. First, it is typically easier to establish an interface between a surrogate model and an optimizer. Second, and more importantly, a surrogate model approach aids parallelization. Optimization is a sequential process and if each function call involves several iterations to converge a highly coupled MDA problem, the overall design time can be long. Instead, with a surrogate model approach, several MDA problems can be evaluated offline and in parallel for different values of the design variables. A surrogate model of the relevant system level objectives and constraints can then be formulated from these converged solutions. If however the design space is too large to efficiently sample, or the interdisciplinary coupling is weak, then a surrogate based approach may not be as advantageous.

F. Overview of Experiments Implementing the Methodology

The Environmental Design Space (EDS) [46] tool is used to implement the proposed methodology. This framework was developed for the US Federal Aviation Administration to assess environmental impacts of aircraft. EDS integrates the aircraft sizing and mission analysis code FLOPS [47], engine cycle analysis code NPSS [48], engine weights and flowpath estimation code WATE++ [49], and other analysis modules for overall vehicle sizing and performance assessment. These industry standard codes have been used for several BLI studies in literature. A series of experiments are proposed to quantify the consequences of ignoring aero-propulsive coupling when designing a BLI vehicle. The experiments aim to show i) decoupled and coupled methodologies show significant differences in vehicle design and performance, thereby demonstrating the need to capture the aero-propulsive interactions ii) differences depend on the relative location of the engine to the wing, which determines the contribution of the wing to the ingested boundary layer properties. As such, two configurations with different engine locations are considered (Fig. 7). The first features a top mounted engine like on the D8, and the other a side mounted like on the NOVA-BLI. Two sets of experiments are conducted on each of the configurations. In experiment 1, block fuel burn estimates between the proposed methodology and a decoupled approach are compared, for a fan pressure ratio and wing loading sweep. Experiment 2 conducts a larger scale design space exploration and optimization study for the same two configurations, considering both cycle and airframe design features, and compares design and performance differences between the two approaches. The following sections walk through the implementation of each stage in the methodology.
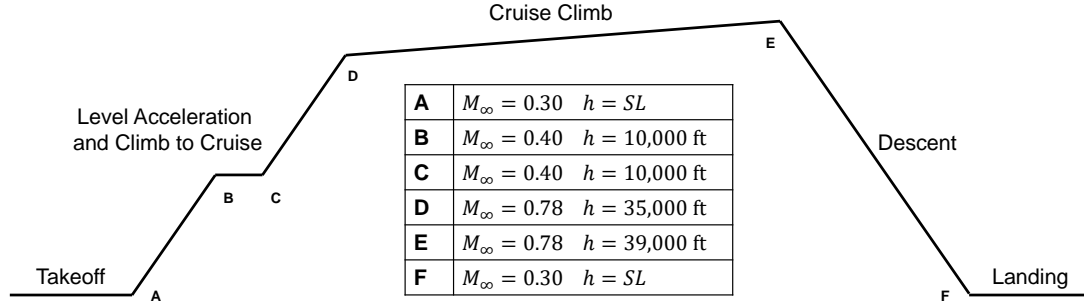
IV. Pre-Vehicle Sizing Stage

A. High Level Requirements and Baseline Aircraft

The main objective is to develop a BLI equivalent of the current 737-8 aircraft, with lower block fuel burn requirements, and an E.I.S. between 2035 and 2040. As such, the current performance capability of the 737-8 is used

to derive several requirements for the BLI version of this aircraft. The aircraft must carry up to 180 passengers, with a twin aisle layout. The twin aisle layout serves two main purposes. First, it enables faster boarding and unloading compared to a single aisle configuration [8, 10], which is an economic incentive for airlines. Second, the wider body enables easier integration of the BLI engines on the fuselage, especially for the top-mounted engine configuration. With a design payload carrying capability of 36,000 pounds, the aircraft must have a design range of 3450 nautical miles, from the payload-range capability of the 737-8 [50]. The design mission of the baseline non-BLI and the resulting BLI aircraft is shown in Fig. 4. The aircraft cruises at $M_\infty = 0.78$, starting at 35,000 ft. and ending at 39,000 ft. The maximum operating Mach number is 0.82. The aircraft must takeoff and land within 8000 ft at standard sea level conditions, assuming both engines are operational, and a dry runway. For context, at these conditions and at TOGW, the 737-8 has a takeoff field length of about 8200 ft. At maximum landing weight, the 737-8 is able to land in about 5800 ft. [50].

A	$M_\infty = 0.30$	$h = SL$
B	$M_\infty = 0.40$	$h = 10,000$ ft
C	$M_\infty = 0.40$	$h = 10,000$ ft
D	$M_\infty = 0.78$	$h = 35,000$ ft
E	$M_\infty = 0.78$	$h = 39,000$ ft
F	$M_\infty = 0.30$	$h = SL$

Fig. 4   Design mission profile for the baseline non-BLI and BLI aircraft

A baseline non-BLI aircraft is created for each BLI configuration. Given differences in the engine location for the BLI configurations, the tail cone design for both is different. At the conceptual level, the only impact this difference has is on the fuselage wetted area calculations, and thus on the fuselage profile drag estimations in FLOPS. The baselines are designed to be similar to a notional 737-8, with key airframe and engine parameters obtained from publicly available data. Other engine and airframe design parameters are calibrated to produce performance and emissions results that are similar to available data. There are some differences however, due to the larger wetted area of the twin aisle fuselage. Important characteristics are summarized in Table 1.

Table 1   Key Characteristics of the Non-BLI Baselines

Parameter	Top Engine	Side Engine	Parameter	Top Engine	Side Engine
S (ft^2)	1379	1377	SLS Thrust/Engine (lbf)	29315	29315
AR	9.22	9.22	TOGW (lbf)	181,140	180,394
$\Lambda_{c/4}$ (°)	25.45	25.45	OEW (lbf)	98,618	98,414
λ	0.303	0.303	Block Fuel (lbf)	38,967	38,502
Fuse. length (ft)	128.3	128.3	TOFL All Engines (ft)	6686	6682
Max fuse. height (ft)	12.9	12.9	LDGFL (ft)	6535	6542
Max fuse. width (ft)	17.6	17.6			
Fuse. wetted area (ft^2)	4926	4657			
ADP FPR	1.539	1.539			
ADP BPR	10.05	10.05			
ADP LPCPR	1.55	1.55			
ADP HPCPR	20.25	20.25			
ADP OPR	47.6	47.6			
d_2 (in)	70.3	70.3			

B. BLI Surrogates Generation Phase

In this sub-stage, surrogate models for $P_{K_{\text{in}}}$, η_{PR}, and $\Delta\Phi_{\text{wake}}$, are generated. In addition, corrections for the fuselage and nacelle wetted areas are also developed to account for $\Delta\Phi_{\text{surf}}$.

1. Define Input Variables and Bounds

Based on the studies presented in [33] and [34], key airframe and propulsor variables affecting the BLI effects were identified. From that, a smaller subset of variables is picked to define the input variable space for the BLI surrogates, summarized in Table 2. The BLI effects directly impacted by a given variable are also listed in this table. The fuselage and nacelle wetted area corrections are only a function of the angle of the fuselage body feeding into the engine (ramp angle: ϕ) and fan diameter. Due to the relative location of the engine and wing, $\Delta\Phi_{\text{wake}}$ due to BLI by the engine is relatively insensitive to wing design changes. Thus, for the $\Delta\Phi_{\text{wake}}$ surrogates, the wing in the geometry model is fixed at the baseline non-BLI aircraft wing design.

Table 2   BLI Surrogate Model Input Variables

Input Variable	LB	UB	Type	BLI Effects
S (ft^2)	1076	1722	Airframe	$P_{K_{\text{in}}}$ and η_{PR}
AR	7	11	Airframe	$P_{K_{\text{in}}}$ and η_{PR}
Λ_{LE} (°)	20	40	Airframe	$P_{K_{\text{in}}}$ and η_{PR}
λ	0.2	0.4	Airframe	$P_{K_{\text{in}}}$ and η_{PR}
ϕ (°)	12	20	Airframe	All
d_2 (in)	68	78	Propulsor	All
SPW_{c_2} (lbm/ft^2-s)	$f(M_\infty)$	44	Propulsor	$P_{K_{\text{in}}}$ and η_{PR}
M_∞	0.25	0.85	Flight conditions	$P_{K_{\text{in}}}$ η_{PR} $\Delta\Phi_{\text{wake}}$
h (ft)	0	43000	Flight conditions	$P_{K_{\text{in}}}$ η_{PR} $\Delta\Phi_{\text{wake}}$
α (°)	0	4	Flight conditions	$P_{K_{\text{in}}}$ η_{PR} $\Delta\Phi_{\text{wake}}$

Bounds on the wing design variables represent a realistic design space for a 150-180 pax aircraft. FLOPS internal aerodynamics work with quarter chord sweep, and thus a mapping is used to translate between quarter chord and leading edge sweep as needed. The ramp angle is changed by changing the cross sectional width (for the side mounted engine configuration) or the cross sectional height of the fuselage at the station just in front of the propulsor highlight. The upper bound is defined to avoid overly thin fuselage cross sections. The lower bound is defined somewhat arbitrarily to ensure a sufficiently high enough value of $P_{K_{\text{in}}}$ for BLI to have a propulsive power benefit. With regards to the propulsor variables, the upper bound on the fan diameter is constrained by the largest propulsor that can adequately fit on the fuselage for a top mounted engine configuration, assuming a two engines. The lower bound is about an inch smaller than the LEAP-1B fan. When considering multiple flight conditions and fan sizes, defining reasonable bounds on mass flow rate is problematic. Specific corrected flow, SPW_{c_2}, is better behaved over the operating envelope, as shown in Fig. 5a.

This figure shows how SPW_{c_2} varies at different operating points in the mission for the baseline non-BLI aircraft. The upper bound on SPW_{c_2} represents max power and is determined by the design SPW_{c_2} assumed when sizing the fan, which is an indirect assumption of the fan blade technology. The smallest values correspond to flight idle conditions. The non-BLI configuration is designed with an assumption that the fan can handle a specific corrected flow of 48 lbm/sqft-s. However, due to blockage effects of the ingested boundary layer, the effective flow area available, for a given fan size, is much smaller. Thus, for the same desired mass flow rate, the effective Mach number of the ingested flow is much higher, which means that the flow is more likely to choke at a smaller mass flow for a BLI propulsor than for a podded propulsor. As such, a more realistic upper bound for the BLI propulsor SPW_{c_2} is 44 lbm/sqft-s. The lower bound for the surrogate model inputs, on the other hand, need not be as low as flight idle conditions. The aircraft lift and associated drag at different points in the mission will result in the engine operating at much higher power settings than idle. As such, one can define the lower bound at a higher specific power code, as shown by the black constraint line in Fig. 5a. Below this constraint, one can assume no BLI effect for lower throttle settings, recognizing that the error in doing so is minimal. This constraint avoids wasting computational resources by sampling in regions that are unlikely to be encountered in a typical mission.

(a) M_∞-SPW_{c_2}

(b) M_∞-h
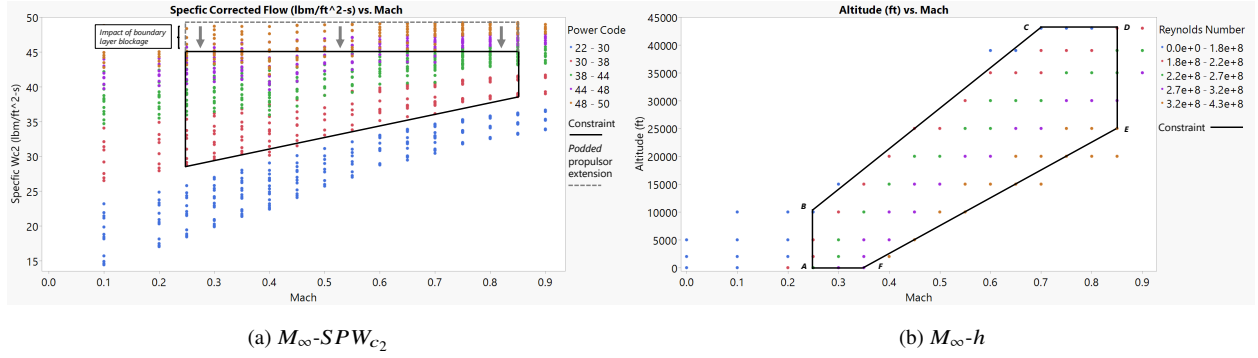
Fig. 5 Operating envelopes for the baseline non-BLI aircraft. Black lines show constraints that restrict this space for the BLI surrogates

A similar strategy can be used to constrain the Mach-altitude operating zone, which is shown in Fig. 5b for the non-BLI baseline. This flight envelope is based on engineering judgment and existing aircraft operations. Black lines show the constrained operating envelope for the BLI surrogates. Lastly, as far as angle of attack goes, the bounds represent a typical range that could be expected at most points in the mission. Since the wing sections are at a non-zero twist, the geometric angle of attack of the wing is different from the aircraft angle of attack specified in Table 2.

2. Define Design Space Sampling Strategy

A design of experiments is created to efficiently sample the design space for a globally accurate surrogate model. It is initially assumed that a standard second order response surface equation will be adequate. If regression analysis indicated a lack of fit, higher order terms or transformations would be considered. Traditionally, Central-Composite or Box-Behnken designs have been used for response surface modeling (RSM). For computer based experiments, space filling designs like the Latin Hypercube Sample (LHS) have been to used to avoid corner points in the design space where computer codes may crash. However, traditional DoEs assume a cubical design space. The irregular nature of the BLI surrogate input space stemming from constraints on the M_∞-h-SPW_{c_2} envelope warrants a computer generated custom design [37]. JMP is an ideal tool for generating such DoEs.

There are several optimality criteria that can be used to assess the quality of the design. One commonly used criterion is the D-optimal condition. D-optimal designs are typically used when the goal is to screen for active design variables [37]. These designs are tailored for precise estimation of the model coefficients. D-optimal designs may be efficient for screening, but since the goal is to generate a globally accurate surrogate, D-optimality is not an adequate criterion to gage the quality of the DoE. In contrast, I-optimal designs are a much better choice. In creating a DoE that maximizes the I-optimality criterion, one is creating a design that minimizes the prediction variance over the entire design space, thereby improving the precision of the predictions made by the surrogate model [37].

Once the optimality criterion is decided, the number of cases must be determined. The smallest number of cases that one can pick for a full second order RSE equals the number of terms in that model. For N design variables, the number of model terms and thus the minimum number of cases to run is given by the equation:

$$\text{Min. Number of Cases} = (N + 1)(N + 2)/2 \qquad (6)$$

However, models generated from such saturated designs typically do not have adequate prediction capabilities. Thus, more samples are needed. However, given the computational cost of each case, an arbitrary number of cases cannot be picked. To determine an adequate number of samples required in the DoE, one can look at the relative prediction variance as a metric. The prediction variance at a design point $\mathbf{x}$, is given by the product of the mean square error (MSE) of the fitted RSM and the relative prediction variance as

$$\sigma^2(\mathbf{x}) = MSE \left[\mathbf{x}^T \left(\mathbf{X}^T \mathbf{X} \right)^{-1} \mathbf{x} \right] \qquad (7)$$

where $\mathbf{X}$ is the matrix of basis functions evaluated at all points in the DoE. The mean square error is dependent on the

11

actual values of the function, $\mathbf{f}$, and the model prediction $\hat{\mathbf{f}}$, and is calculated as follows:

$$MSE = ||\mathbf{f} - \hat{\mathbf{f}}||^2/N \tag{8}$$

Evident from Eq. (7), the relative prediction variance is solely dependent on the DoE. The objective is to pick the right number of cases such that the relative prediction variance is reduced. The surrogates for $P_{K_{in}}$ and η_{PR} are a function of 10 design variables. From Eq. (6), one sees that these surrogates require a minimum of 66 samples. For the $\Delta\Phi_{\text{wake}}$ surrogates, there are a total of 5 variables. However, since d_2 can be changed easily without requiring an additional CFD run, this variable can be dropped from the DoE size calculations. Thus, the minimum number of cases required is 15. Fig. 6 shows the fraction of design space plot for the two DoEs. These plots compare the relative prediction variance over the design space for the smallest possible DoE, against larger DoEs with more cases. The best design is one that minimizes the relative prediction variance over a larger fraction of the design space, while minimizing the number of cases needed. Diminishing returns are evident in Fig. 6, where the reduction in relative prediction variance over the design space, per 10 additional cases, decreases. Thus, for $P_{K_{in}}$ and η_{PR} surrogates, 96 cases appears to be adequate, while for $\Delta\Phi_{\text{wake}}$, 27 cases are sufficient. Note that for $\Delta\Phi_{\text{wake}}$, d_2 will be changed thrice per CFD run. So while the total CFD runs required is 27, the number of samples in the DoE will be 81. An additional 20 cases for $P_{K_{in}}$ and η_{PR} and 9 CFD runs for $\Delta\Phi_{\text{wake}}$ are conducted for validating the surrogate models.

(a) For $P_{K_{in}}$ and η_{PR} (b) For $\Delta\Phi_{\text{wake}}$
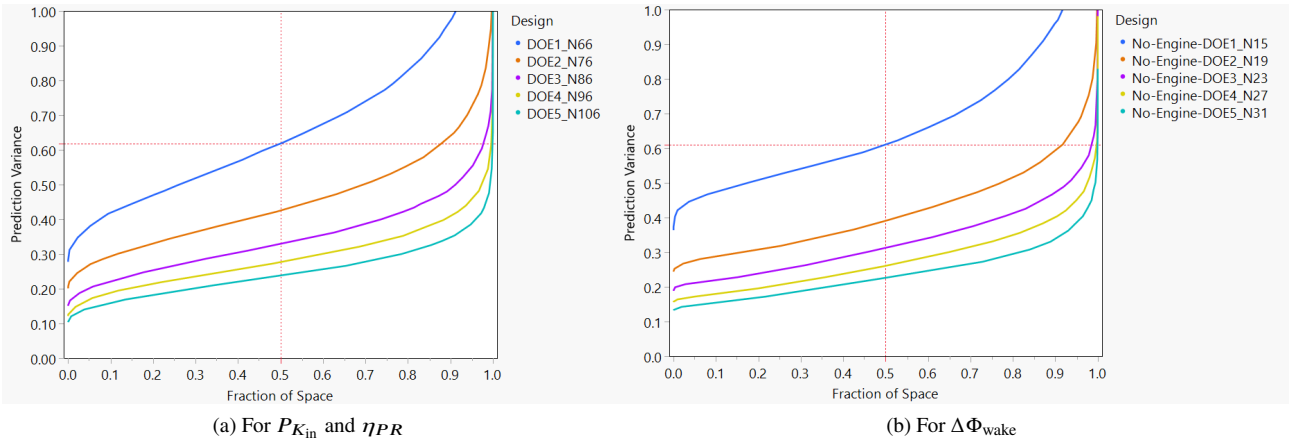
Fig. 6 Fraction of design space plot comparison of the five DoEs considered for the three BLI effects. The yellow curve shows the relative prediction variance for the chosen DoE

The fuselage and nacelle wetted areas calculated by FLOPS, for an input set of fuselage and engine dimensions, can be overwritten by user specified values for SWETF and SWETN respectively. If either quantity is less than 5, then the term is treated as a multiplier, otherwise, it is considered as a dimensional quantity for wetted area. Wetted and theoretical area calculations for each component can be obtained from OpenVSP. There are 9 unique combinations of d_2 and ϕ in the training DoE for $P_{K_{in}}$ and η_{PR}. These 9 points are used for training the SWETF and SWETN surrogates. For SWETF and SWETN validation, the first 9 points in the validation DoE for $P_{K_{in}}$ and η_{PR} are used. SWETF is specified as a dimensional quantity. SWETN on the other hand is calculated as a ratio of the wetted area to theoretical surface area of the nacelle. This quantity captures the reduction in surface area due to partial embedding of the nacelle in the fuselage. SWETN then corrects FLOPS's estimation of the nacelle wetted area, which is based on engine dimensions calculated by WATE++.

3. Prepare Geometry and CFD Models to Evaluate BLI Effects

The next step in generating the BLI surrogates is defining appropriate geometry models for the aircraft. OpenVSP is used to create a template for each configuration, as shown in Fig. 7. These templates are then modified for each case in the DoE. As seen in experiment 5 in [33], the fuselage length and cross sectional area are key parameters affecting the BLI effects. The length of the fuselage is based off a notional 737-8. The fuselage cross sectional design was driven by the need to fit two BLI engines on top of the fuselage. As such, this cross section is based off a notional D8, where the cross sectional area of the fore section is matched to values available in literature, and the shape is approximated by a
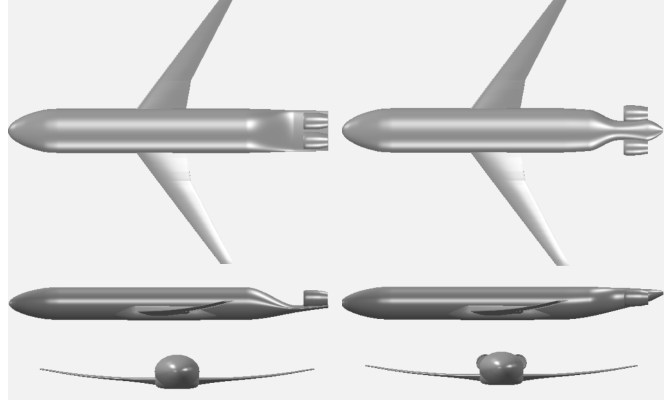
Fig. 7   3-views of the templates that are used for generating the geometry models for each DoE case

'sideways ellipse', which on the basis of experiment 5 in [33], is an adequate representation. Both configurations share the same cross section up until the tail cone region, which is modified to integrate the engines.

A simplified representation of the fuselage nose is used since experiment 2 in [33] shows that this simplification, for shock free cases, has a negligible impact on the BLI effects. A belly fairing is included to minimize the impact of flow separation at the wing root-fuselage junction on the BLI effects, as shown in experiment 6 in [33]. Both templates share the same wing design, which is the scaled CRM wing that was used as a reference in experiment 6 in [33]. No empennage is included in the templates since the impact of the tails is mostly on the fuselage trailing edge mounted propulsor, which is not considered in this study. However, the *y* location of the engine and the maximum diameter are constrained for the top mounted engine configuration to integrate a vertical tail on the sides, like on the D8 concept. Experiment 8 in [33] highlighted the relative significance of the ramp angle over the skinning angles, as long as the skinning angle settings do not produce a local separation bubble. As such, the skinning angles are somewhat arbitrarily set to smoothen the transition between the fuselage and the ramp, but are not part of the design space.

Following the geometry model definition, the CFD cases have to be set up. STAR-CCM+ is used for the CFD simulations. Steady state conditions and standard atmosphere properties are assumed. An unstructured Cartesian mesh is used. A grid refinement study is conducted for the top-mounted engine configuration to find an appropriately sized mesh that balances accuracy and computational expense. This study is conducted at $M_\infty = 0.8$, $h = 35,000$ft and $\alpha = 2.0$. The wing design parameters and fan diameter are set at the non-BLI baseline values. The results of the grid refinement study are shown in Fig. 8. The final mesh chosen is shown with a filled marker. The maximum variation in $C_{P_{K_{\text{in}}}}$ $(P_{K_{\text{in}}}/q_\infty V_\infty S_{\text{ref}})$ for finer meshes relative to the chosen mesh, when dimensionalized to a force, is approximately 1 lbf. For η_{PR}, this variation is approximately 0.01% and for $\dot{m}$ it is about 0.04%. These variations are quite small and do not warrant the use of a finer mesh.

(a) $C_{P_{K_{\text{in}}}}$ and η_{PR}

(b) $\dot{m}$
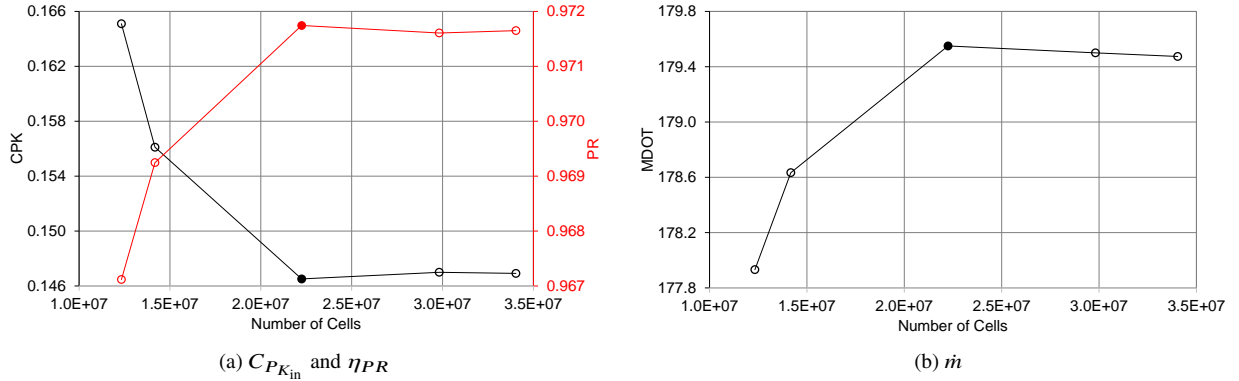
Fig. 8   Summary of results from mesh sensitivity trials

4. Generate Surrogate Models and Evaluate Quality of Fits

Once the CFD cases are run for each point in the DoE, surrogate models can be fit to the responses. There are certain qualitative and quantitative diagnostic measures to evaluate the validity of generated surrogate models. These are listed as below. Each metric in isolation provides useful information about a surrogate model, but, a holistic view is required to determine the validity of this model.

- R^2 metrics
- Average error as a fraction of the mean response
- Actual vs. predicted trends
- Residual vs. predicted trends
- Model fit error (MFE) distribution
- Model representation error (MRE) distribution
- Evaluate predicted trends against expected results obtained from previous experiments or physics based reasoning

The R^2 metric is a commonly used quantitative measure of how well the assumed model measures variability of the input data. This metric can be evaluated for both the data used to fit the surrogate model and that used to validate it. A surrogate model that perfectly interpolates the input data, which occurs when the number of terms in the model equals the number of data points, has $R^2 = 1$. In general, when there are more data points than model terms, as is the case with the BLI surrogates, $R^2 < 1$. Low values of R^2, such as say $R^2 < 0.6$-0.7 is indicative that the assumed model form for a given response is lacking in accuracy. As a general rule of thumb, high values of R^2, typically above 0.9, are desirable. However, it should be emphasized that when looking at R^2, one must consider the training and validation data separately. A surrogate model that has low error in fitting the training data will have a high R^2-Training result, but, may suffer from over fitting. In this scenario, the model predictions at data points not used for training the surrogate may be completely inaccurate due to the model overshooting the actual value. As such, R^2-Validation is severely penalized. Thus, when training the surrogate model, one must also track how well the model predicts previously unseen data, and thus, both R^2-Training and R^2-Validation greater than 0.9 are recommended. Typically, R^2-Training is higher than R^2-Validation. Table 3 shows the R^2-Training and R^2-Validation values for the BLI surrogates, calculated automatically by JMP. Most values are around 0.98 and above, except R^2-Validation for $\Delta\Phi_{\text{wake}}$ at 0.967, thus satisfying the R^2 criterion.

R^2 by itself, however, is not sufficient to indicate model accuracy. One must also look at other metrics. Another quick diagnostic is to check the root average square error (RASE) as a percentage of the mean response for both the training and validation data. RASE is calculated as the square root of the sum of squared prediction errors divided by the number of observations. A more accurate model minimizes this percentage error. RASE-Training is typically

Table 3 BLI Surrogate Models R^2 and RASE Metrics

Engine	Metric	$P_{K_{\text{in}}}$*	P_{t_2}	$\Delta\Phi_{\text{wake}}$*	SWETF	SWETN
	R^2 Training	0.9987	0.9999	0.9973	1	1
	R^2 Validation	0.9899	0.9995	0.9670	1	1
	RASE Training	0.038	180	0.034	0.002	1×10^{-5}
Top	RASE Validation	0.076	574	0.074	0.057	2×10^{-5}
	Mean Response	6.45	64354	3.39	4927	0.846
	RASE-Train %Mean	0.59	0.28	1.00	4×10^{-5}	1×10^{-3}
	RASE-Val %Mean	1.18	0.89	2.18	1×10^{-3}	2×10^{-3}
	R^2 Training	0.9937	0.9999	0.9964	1	1
	R^2 Validation	0.9840	0.9996	0.9893	1	1
	RASE Training	0.087	172	0.038	0.010	2×10^{-6}
Side	RASE Validation	0.094	480	0.049	0.036	2×10^{-5}
	Mean Response	6.06	63654	3.67	4656	0.904
	RASE-Train %Mean	1.43	0.27	1.04	2×10^{-4}	2×10^{-4}
	RASE-Val %Mean	1.55	0.75	1.33	8×10^{-4}	2×10^{-3}

*These responses are transformed to an equivalent force and then the natural log of the result is used as a response

lower than RASE-Validation. An error of less than 2% is desirable, with values closer to 0 being ideal. Table 3 shows the RASE and mean response values calculated by JMP for each BLI surrogate. Barring RASE-Validation for the top-engine configuration $\Delta\Phi_{\text{wake}}$ model, all errors as a fraction of the mean response are well below 2%.

The next two diagnostics are more qualitative measures of goodness of fit. The actual vs. predicted plot, as the name suggests, shows the distribution of the actual or true response plotted against the predicted response from the surrogate model. The ideal line of fit is a 45 degree line where the actual and predicted responses are identical. The distribution of points along this ideal fit line is a qualitative indicator of model adequacy. A surrogate model with low prediction error has a tighter fit of points around this ideal fit line, and is evenly distributed along this diagonal without obvious clumping of data points. The residual vs predicted plot on the other hand provides a different perspective on the same data by plotting the residual value (error between the predicted and actual value) against the predicted response. An ideal plot shows random scattering of points that have a residual that is at least an order of magnitude lower than the predicted response. These two plots combined can also indicate the need for higher order terms in the model, or transformations to the response, based on how well the distribution of points agrees with the ideal scenario. An example of poor and acceptable fits can be seen in Fig. 9 generated by JMP.

$$C_{P_{K_{\text{in}}}}$$

$$\ln\left(C_{P_{K_{\text{in}}}} q_\infty S_{\text{ref}}\right)$$
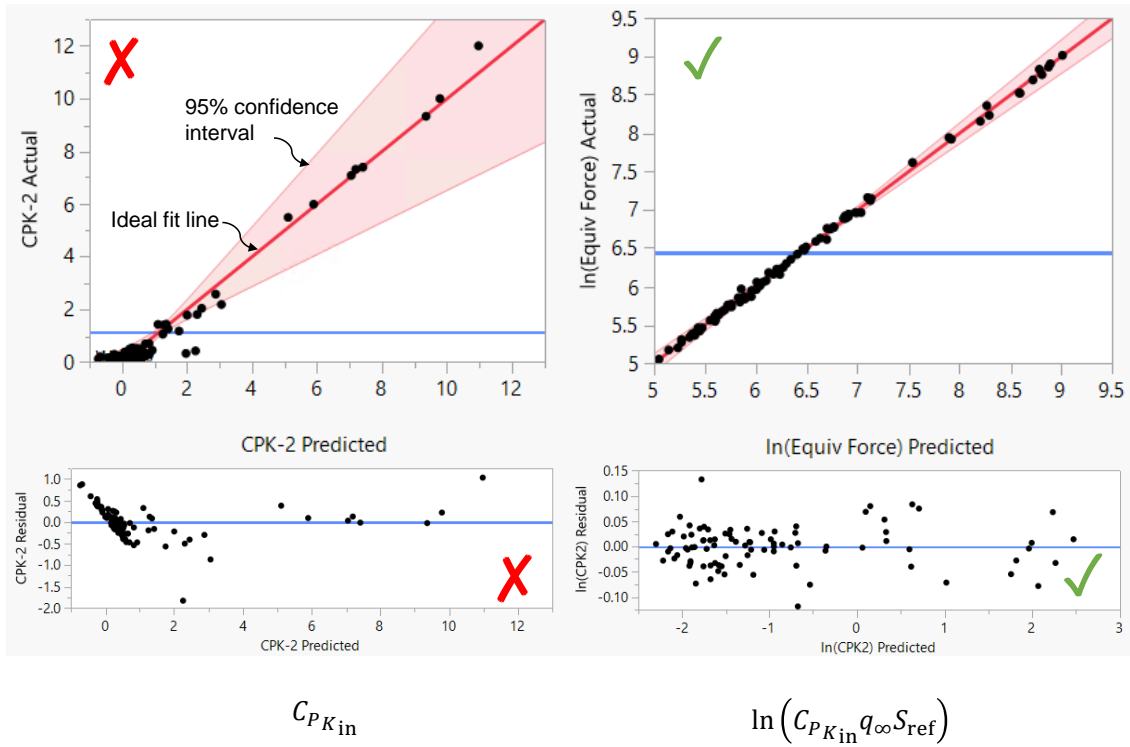
Fig. 9   Actual vs. predicted and residual vs. predicted plots for the top mounted engine $P_{K_{\text{in}}}$ surrogate comparing a poor vs. acceptable fit

In Fig. 9, the second order response surface fit is shown for $C_{P_{K_{\text{in}}}}$ on the left and the transformed response on the right. The actual vs. predicted plot for $C_{P_{K_{\text{in}}}}$ shows a clumping of points at the bottom corner, a few outliers, and a wide confidence interval around the ideal fit line, indicating poor statistical significance of the assumed model for this response. The residual vs. predicted plot shows a distinctive clumping pattern, and the residuals are also on the same order as the predicted response. Both these plots indicate a poor fit for $C_{P_{K_{\text{in}}}}$, suggesting the need for a transformation. By converting the non-dimensional BLI effect to an equivalent force, and then taking the natural log of this metric, the second order response surface equation is now a much better model for this transformed response. The actual vs. predicted and residual vs. predicted plots are acceptable based on the diagnostics discussed above. The confidence interval is much smaller and the residuals are one to two orders of magnitude smaller than the predicted response. Similar transformations are required for $\Delta\Phi_{\text{wake}}$ to improve the fit. For η_{PR}, it is found that p_{t_2} is a better metric to fit a standard second order RSM. In general, the plots for all transformed BLI responses indicate adequate fits, with the $P_{K_{\text{in}}}$ response for the side engine case showing the largest spread in the residuals.

The last statistical diagnostic measures are the MFE and MRE distributions. The MFE distribution shows the relative error of the model with respect to the actual values, for the points used to train the surrogate. The MRE distribution on the other hand shows the same information, but for the points used to validate the model. These two distributions basically provide a quantitative perspective of the data in the actual vs. predicted and residual vs. predicted plots, categorized by training and validation samples. A good second order RSM is one that has an MFE histogram resembling a standard normal distribution, with a mean of zero, a standard deviation of 1%, and a range of ±3%. These criteria imply that the error in neglecting higher order terms in a second order RSM is acceptable. The MRE distributions on the other hand typically show a larger variation. Outliers will affect the standard deviation and range of these distributions. These should be investigated to determine whether they can be ignored or not. For all BLI responses modeled, the mean percentage error is close to zero. The standard deviations for the training data for all responses is either less than 1%, or marginally over 1%, with the $P_{K_{in}}$ surrogate for the side engine showing the largest standard deviation at 1.4%. The upper bound on percentage error for this response is around 3.4%, while the lower bound for this response is 2.97%. All remaining responses have an error range well within ±2-3%. The MRE plots show larger variations, as expected. However, the error range is still within 3%, the mean errors are still close to zero, and the standard deviations, though larger than those for the MFE, are in most instances below 1.5%.

Lastly, in addition to the statistical measures of goodness of fit, it is also helpful to see if the predicted trends make sense from a physics perspective. Fig. 10 presents profiler plots generated by JMP that show a snapshot of the BLI effects trends against the input variables, at a user specified design and operating point. These profilers are generated from the fitted surrogate models for the side-engine configuration. The chosen point can be interactively varied, and the observed trends change depending on the non-linearity of the response and interaction effects between the variables. The design and operating point shown in Fig. 10 is chosen to match the conditions at which the experiments in [33] and [34] were conducted. This way, trends from these experiments can help shed light on the reasonableness of the predicted response. While the profiler plots show dimensional forces and pressure, for a fixed Mach and altitude these dimensional values carry the same information as their non-dimensional counterparts investigated in [33] and [34].

The direction of the BLI effects trends with wing design changes agree with those seen in experiment 6, in [33]. In addition, the opposite correlations of $P_{K_{in}}$ and pressure recovery with wing design changes, as expected and observed in experiment 6, is captured by the surrogate models. Trends with ramp angle, for all three BLI effects, also agree with findings from experiment 8 in [33]. The decrease in $P_{K_{in}}$ and pressure recovery, with an increase in flow rate or a decrease in fan diameter, agrees with results from experiment 1 in [34]. Mach and altitude trends observed are also consistent with physics. One expects a reduction in the equivalent force benefit going up in altitude for a fixed Mach number, or lowering Mach number at the same altitude, due to dependency of dimensional force on freestream dynamic pressure. Mach and Reynolds number effects on the boundary layer also explain p_{t_2} trends with flight conditions. These trends, in conjunction with the statistical diagnostic information discussed above, show strong support for the validity of the developed BLI effects surrogate models.
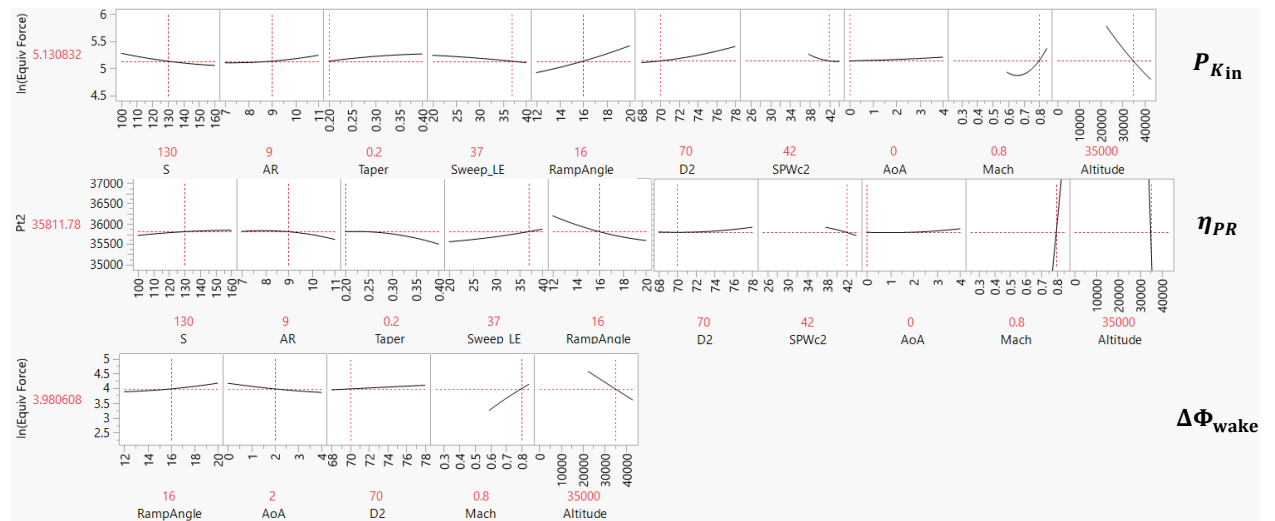
Fig. 10 Profiler plots showing trends for the side-engine configuration, at a given design and operating point

V. Vehicle Sizing Loop and Experiment 1

This section describes how the BLI coupled and decoupled methodologies are implemented for aircraft sizing in the EDS framework. The focus is on how the BLI surrogates are integrated and used within this design environment. Fig. 11 compares the XDSM of the coupled BLI vehicle sizing methodology to the decoupled approach. The order of the processes is indicated by the numbering, as is standard XDSM convention. The processes depicted in the diagrams are described in the following sub-sections.
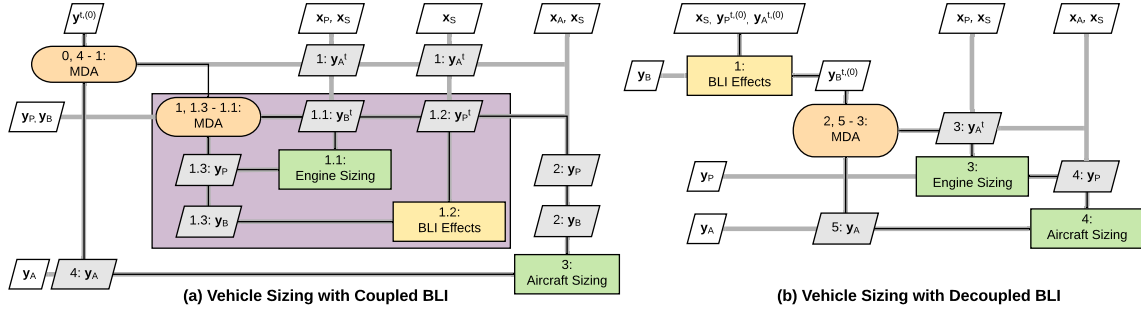
Fig. 11   XDSMs comparing the coupled and decoupled BLI effects accounting approaches for vehicle sizing

A. Coupled BLI Sizing

The BLI aircraft sizing loop begins with a specification of airframe parameters, $\mathbf{x}_A$, engine parameters, $\mathbf{x}_P$, and parameters shared by the engine, airframe, and BLI effects models, $\mathbf{x}_S$, in a csv file. Initial guesses for the coupling variables related to each discipline $\mathbf{y}^{t,(0)}$ are also specified in this file. These parameters are used as inputs for NPSS, FLOPS, WATE++, the BLI surrogates, and other disciplinary analysis tools in EDS. In addition to the csv input file, there are files defining the engine architecture for NPSS and a baseline aircraft model file for FLOPS. Table 4 highlights what kind of variables each of the above vectors represent. Note that the list of airframe and propulsor design variables shown in Table 4 is not exhaustive. The shared and coupling variable lists, however, are complete.

Initial values for $\mathbf{x} \equiv \{\mathbf{x}_A, \mathbf{x}_P, \mathbf{x}_S\}$ are provided by the non-BLI baseline obtained in the pre-vehicle sizing stage. These values are fixed for the sizing process. The first process in Fig. 11a is the engine design loop (process 1), which involves a feedback between engine sizing and the evaluation of BLI effects. The engine is sized using a multi-design point approach, as stated previously. The design points are: 1) Aerodynamic Design Point (ADP) 2) Top of Climb (TOC) 3) Takeoff (TKO) 4) Sea Level Static (SLS). Each design point requires a specification of the flight Mach number, altitude, deviation from standard atmosphere temperature (which is set to zero for these cases) and a design thrust required. ADP is set at $M_\infty = 0.8$ and $h = 35,000$ ft. TOC is also set at the same flight conditions, but involves operating the fan at a higher speed. TKO and SLS are set at sea level, but TKO is defined at $M_\infty = 0.25$, while SLS is by definition

Table 4   Examples of Design Parameters and Coupling Variables

Parameter	Examples
$\mathbf{x}_A$	Empennage volume coefficients, empennage: AR, λ, $\Lambda_{c/4}$, wing dihedral, component weight factor estimations: avionics, APUs, etc., component lengths, wing loading, thrust to weight ratio, etc.
$\mathbf{x}_P$	FPR, BPR, HPCPR, LPCPR, maximum fan specific flow, compressor and turbine hub to tip ratios, component efficiencies, assumed turbomachinery design characteristics like number of blades, aspect ratio, etc. for weight calculations, assumed duct losses, $T_4^{\max}$, etc.
$\mathbf{x}_S$	Wing: AR, Λ_{LE}, λ, ramp angle ϕ, flight conditions
$\mathbf{y}_A$	Wing planform area and thrust scaling factor (or thrust requirements at engine design points)
$\mathbf{y}_P$	Fan diameter, max nacelle diameter, engine length, engine weight, engine deck
$\mathbf{y}_B$	$P_{K_{\mathrm{in}}}$, η_{PR}, $\Delta\Phi_{\mathrm{wake}}$, fuselage wetted area (SWETF), nacelle wetted area (SWETN)

at static conditions. The initial thrust requirements at these points, contained in $\mathbf{y}_A^t$, are meant to represent expectations of the vehicle performance at these flight conditions. A more accurate initial guess results in fewer iterations between NPSS and FLOPS.

For a given set of $\mathbf{x}_P$ and $\mathbf{y}_A^t$, NPSS designs an engine that meets the design requirements. The BLI effects, contained in the vector $\mathbf{y}_B$, are integrated in different ways. The mapping between thrust-drag and power balance allows for the BLI effects $P_{K_{in}}$ and $\Delta\Phi_{wake}$ to be accounted for as an equivalent force benefit. This effective force is tacked on to the gross thrust calculations for the engine. The η_{PR} losses from the BLI surrogates are used to overwrite default inlet performance curves. The BLI surrogates are part of the engine model and are evaluated simultaneously with the cycle analysis in this iterative process. There is a set of surrogates per configuration, and if-statements are used to select the appropriate models based on the engine location. While the surrogate input bounds were set previously to capture a reasonable design and operation space, checks are imposed within the environment to make sure there is no extrapolation from the BLI surrogate models. In particular, for flow rates below the surrogate lower bounds, the BLI gross thrust correction is set to zero, and the pressure recovery values are calculated from the built in inlet performance curves. Additionally, since the fan is oversped at TOC, the specific flow at that condition is marginally higher than the specified design value. To prevent extrapolation beyond the upper limit of 44 lbm/ft^2-s, the maximum design SPW_{c_2} is set to 43 lbm/ft^2-s such that even at overspeed conditions, the maximum SPW_{c_2} is within the BLI surrogate bounds. Note that these SPW_{c_2} values are based on standard atmosphere conditions. The 'Ambient' element in NPSS allows for specification of the flight Mach number and altitude, and can map these conditions to standard atmosphere properties.

While the BLI effects surrogates are a function of angle of attack, this variable is not recognized by any of the disciplinary analysis codes in EDS. All drag polars in FLOPS are specified in terms of C_D and C_L. Thus, one must provide an estimate for the operating angle of attack at any given point in the mission for the BLI surrogates. One way of doing so is to specify an h-α schedule. Within the range of 0°-4°, higher aircraft angles of attack are likely to be found at low altitudes during takeoff and climb. As the aircraft approaches cruising altitude, the angle of attack is expected to decrease. As such, a step function approach is adopted where for any operating point below 10,000 ft., α is assumed to be 4°. Between 10,000 and 30,000 ft. α is assumed to be 2° and for higher altitudes where the aircraft will cruise, α is set to 0°. Given the sensitivity of the BLI effects to α, discussed in [33], changes to this schedule will impact the fuel burn estimate of the BLI vehicle relative to the non-BLI counterpart. However, since the same schedule is used for all experiments, coupled and decoupled, the impact of α on the conclusions drawn with regards to the differences between coupled and decoupled are unaffected. This claim is supported with an α sensitivity study in experiment 1.

After the engine has been sized for an initial set of thrust requirements and BLI corrections, off design analysis generates the engine decks to be used by FLOPS. In addition, WATE++ provides estimates for the engine weight and critical dimensions. The pylon weight for a non-BLI configuration is calculated based on a fixed fraction of the total engine weight. For the BLI configurations without a python, this weight is set to zero. The engine dimensions provided by WATE++ are used by FLOPS to calculate the nacelle drag, however, the SWETN surrogate developed previously corrects the nacelle wetted area based on the sized fan diameter and inlet ramp angle. The fuselage wetted area is provided from the SWETF surrogate. FLOPS sizes the airframe for the specified wing loading, thrust to weight ratio, mission, range constraint, and other airframe design parameters. Based on the gross weight converged on by FLOPS and the user specified wing loading, the wing is resized from the initial guess. This new value is passed back to the surrogates in the subsequent iteration. In addition, the engines are rescaled if they produce more thrust than required for the mission, or are unable to meet the thrust requirements. This scaling factor is applied to the thrust requirements at the engine design points for the next sizing iteration. The sizing iteration converges when Eq. (5) is satisfied. For the wing area, the convergence tolerance is set to 5ft^2.

The only inputs to the BLI effects surrogates that change in the sizing process are d_2, and S. The fan diameter changes within both process 1 (as part of engine on-design) and as part of process 0 (when the engines are scaled based on airframe performance). The planform area only changes in the outer MDA loop (process 0). For the *coupled BLI sizing, both d_2, and S inputs to the surrogate models are updated with each iteration.* The fan diameter updates affect all five BLI effects surrogates in $\mathbf{y}_B$ while the planform area updates affect $P_{K_{in}}$, η_{PR}, and $\Delta\Phi_{wake}$.

B. Decoupled BLI Sizing

The decoupled approach shown in Fig. 11b is intended to be reflective of the decoupled methods described in literature for BLI modeling. In particular, the system level study for the BWB by Hardin [51] and the STARC-ABL vehicle design study by Welstead [6] are prime examples of this decoupled approach. Both these studies relied on an handful of CFD solutions for the boundary layer, from a fixed aircraft geometry, thereby ignoring the aero-propulsive

coupling. To mimic these approaches with the BLI surrogate models, the disciplinary coupling variable inputs to the surrogates: d_2 (in $\mathbf{y}_P^{t,(0)}$) and S (in $\mathbf{y}_A^{t,(0)}$), are fixed at their initial guessed values. These quantities are not updated over the course of the sizing loop. The operating condition inputs are allowed to vary for the surrogates, since the decoupled approaches in literature did account for these conditions in some manner. *It should be emphasized that the decoupled approach here solely refers to the treatment of the BLI effects on the aircraft design, and not the entire sizing process.* The engine size is still scaled with the aircraft in an iterative manner as before. It is just that the BLI effects are not corrected for the changing aircraft size.

The differences in aircraft design and performance between the decoupled and coupled approaches ultimately depend on the initial guess provided for d_2 and S. If these are close to the values that are obtained from the coupled approach, then naturally, the differences will be smaller. However, it is not always easy to estimate what the coupled design would look like without actually accounting for the BLI aero-propulsive coupling. A reduction in wetted area, engine pylon weight, along with $P_{K_{in}}$ and $\Delta\Phi_{wake}$ reduce engine thrust requirements, allowing for a smaller engine. However, boundary layer blockage effects need to be accounted for, and the drop in engine performance due to a loss in pressure recovery both tend to result in a larger fan diameter. The larger engine is heavier, has more wetted area, which tends to increase the thrust requirements, counteracting some of the aforementioned benefits. While a larger area implies more BLI, this is not necessarily optimal for performance. Additionally, changes in fuel and engine weight also affect the wing size, which in turn has a direct impact on both aircraft drag and the BLI effects. Given all these competing interactions, a justifiable initial guess for d_2 and S would be that obtained from an equivalent non-BLI baseline. This strategy would be consistent with the decoupled approaches in literature, where the CFD profiles were obtained from a representative non-BLI aircraft. If BLI related aero-propulsive coupling is weak, then the final d_2 and S for the BLI aircraft (with a decoupled or coupled approach) will be close to the non-BLI baseline. If the coupling is stronger, more significant differences are expected, justifying the need for the methodology proposed in this paper.

C. Experiment 1: MDA Sweeps

In these experiments, first, design FPR is varied between 1.48 and 1.60 for a constant value of wing loading (WSR) at 131.4 lbf/ft^2, for the non-BLI and BLI versions of both aircraft configurations. The ranges for FPR are determined based on expected variations in d_2. The fan diameter cannot be outside the 68-78 in. range for the BLI configuration. Then, WSR is varied between 115 to 145 at a fixed FPR of 1.54. The non-BLI configurations are analyzed first. The sized d_2 and S for each case are used as inputs for the decoupled-BLI runs. The metric of interest, design block fuel, accounts for fuel burn during the design mission and during taxi in, but not reserves. Different people make different assumptions regarding the reserve mission with respect to the distance to the nearest airport, maximum cruising altitude, speed, etc. While a 200 nautical mile reserve mission is specified when sizing both the BLI and non-BLI aircraft, the fuel burn for this mission is not considered for the experiments. Fig. 12 shows the block fuel requirements for the top-engine configuration for the non-BLI, BLI-decoupled, and BLI-coupled variants, while Fig. 13 shows the same for the side-engine configuration. A few comments on the general fuel burn trends with FPR and WSR can be made first, before focusing on the differences between the coupled and decoupled trends.

(a) FPR sweep for WSR=131 lbf/ft^2 (b) WSR sweep for FPR = 1.54
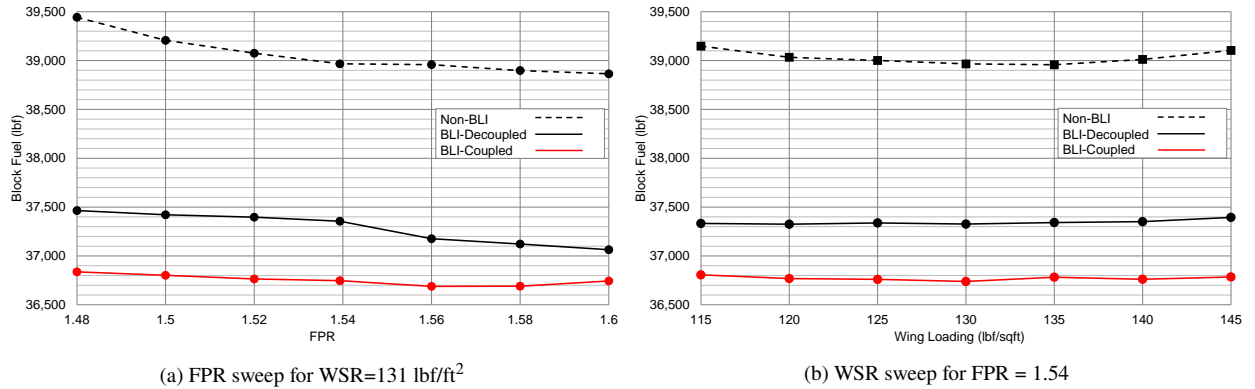
Fig. 12   Experiment 1: Block fuel requirements for the non-BLI, BLI-decoupled, and BLI-coupled variants of the top engine configuration as a function of design FPR and WSR

(a) FPR sweep for WSR=131 lbf/ft^2 (b) WSR sweep for FPR = 1.54
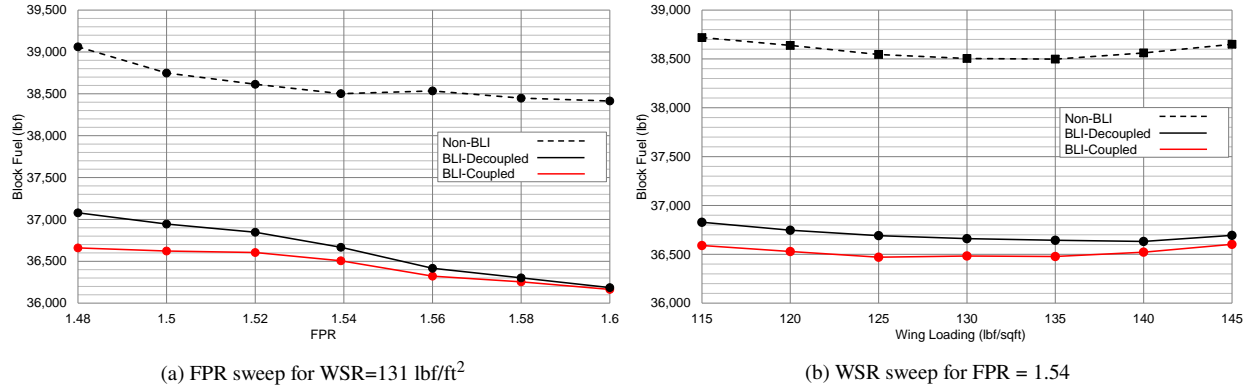
Fig. 13 Experiment 1: Block fuel requirements for the non-BLI, BLI-decoupled, and BLI-coupled variants of the side engine configuration as a function of design FPR and WSR
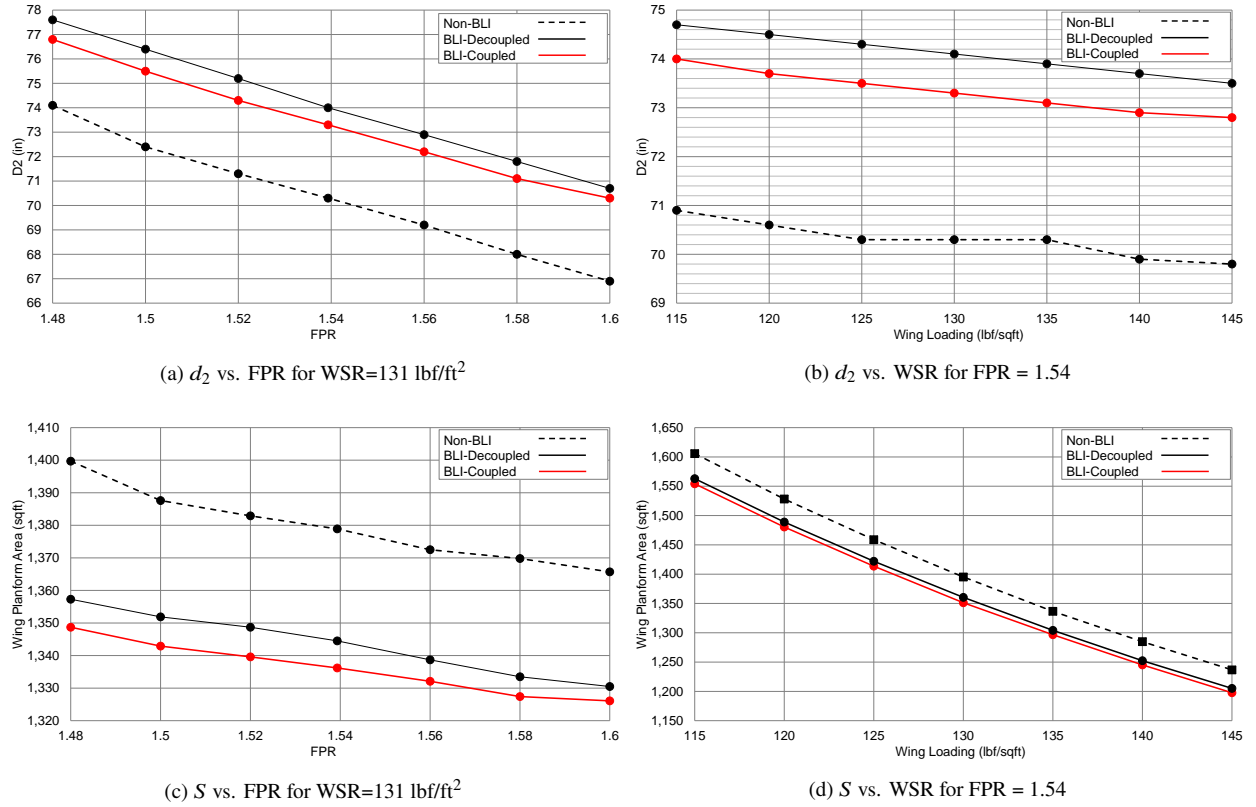
In all cases, fuel burn savings going from the non-BLI to the BLI variant is observed, as expected. With regards to FPR, both the BLI and non-BLI variants exhibit similar trends. Typically, for a large variation in FPR, a fuel burn bucket is observed, where the fuel burn is minimized at some FPR value. Moving away from that point in either direction results in an increase in fuel burn. The aerodynamic penalties of large nacelles for low FPR engines outweigh the propulsive efficiency benefits, resulting in an increase in fuel burn with a decrease in FPR. This trend is observed in both Fig. 12 and Fig. 13. The BLI vehicle fuel burn increase with a decrease in FPR is much flatter for lower FPR values, compared to the non-BLI vehicle. This behavior is explained by the BLI benefit from larger fans offsetting the aerodynamic penalty to a certain extent, which is obviously not a factor for the non-BLI variant. On the other end, the lower propulsive efficiency of high FPR engines eventually outweighs the aerodynamic benefits of smaller engines, resulting in an increase in block fuel with an increase in FPR. This behavior is not observed in the results because the upper bound of FPR considered, based on the fan diameter constraint, is not high enough for the propulsive efficiency penalties to dominate. Fuel burn trends with wing loading are again similar for both BLI and non-BLI variants and exhibit a bucket, which suggests an optimal wing size and aircraft weight combination. The fuel burn increase in either direction of the optimal is due to a combined effect of changes in aircraft weight due to sizing effects, which affects the required C_L, changes in wing size and weight, and the corresponding airframe drag resulting from the aerodynamic efficiency of the wing to produce the required C_L.

Now, with regards to the differences between the coupled and decoupled methods, there are two main takeaways from Fig. 12 and 13:

1) There are significant differences in block fuel burn for a fixed range constraint if one uses a decoupled approach instead of a coupled

2) These differences are more pronounced for the top-mounted engine, given the wing influence on the ingested inflow, as shown in [33]

The decoupled approach consistently over-predicts the block fuel requirements for these cases, compared to the coupled method. The initial guesses for d_2 and S that are provided to the decoupled approach, from the non-BLI variants, result in an under-estimation of the BLI effects. As a consequence, the aircraft is over sized, as hypothesized. The converged d_2 and S for the decoupled BLI aircraft are larger than those predicted by the coupled approach, as seen in Fig. 14 for the top-engine configuration. Conversely, if the d_2 and S inputs to the BLI surrogates for the decoupled approach were higher than the converged results from the coupled approach, the BLI benefit would be over-predicted. Consequently, the final converged values of d_2 and S for the decoupled approach would be lower than the coupled results. The discrepancy between the decoupled and coupled approaches is the smallest when either the initial d_2 and S inputs for the BLI surrogates are close to the converged coupled values, or, when the BLI related aero-propulsive coupling is weaker, as evident in the side engine block fuel results in Fig. 13, and the comparison of the final d_2 and S values for the aircraft in Fig. 15.

The results in Fig. 15 suggest that while BLI does have an impact on the sized vehicle, based on the difference between the BLI and non-BLI curves, the aero-propulsive coupling due to BLI is a lot weaker than observed for the top-engine configuration. As a result, even though the non-BLI values of d_2 and S, which are used as inputs for the

20

(a) d_2 vs. FPR for WSR=131 lbf/ft^2

(b) d_2 vs. WSR for FPR = 1.54

(c) S vs. FPR for WSR=131 lbf/ft^2
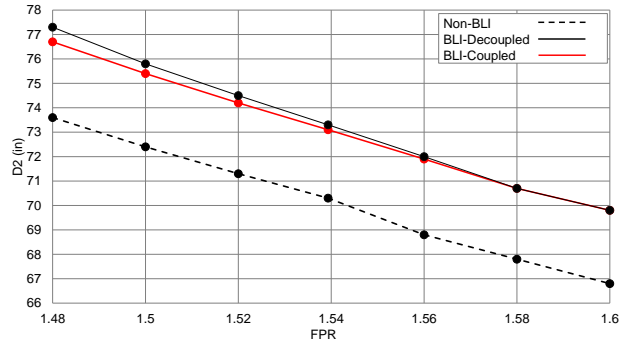
(d) S vs. WSR for FPR = 1.54

Fig. 14   Experiment 1: Variations in d_2 and S vs. FPR and WSR for the top engine non-BLI, decoupled-BLI, and coupled-BLI configurations

decoupled approach BLI surrogates, are considerably different from the converged BLI results, variations in d_2 and S as part of the sizing process have a smaller impact on the BLI effects for this engine location. Thus, the coupled approach results are not much different from the decoupled approach. Another interesting observation is that the discrepancy between the coupled and decoupled approaches reduces with an increase in FPR and WSR (a decrease in d_2 and S). For larger fans, there is more BLI. Thus, the d_2 and S inputs based off the non-BLI configuration, are further away from the 'true' converged solutions from the coupled approach. For smaller fans with less BLI, relative variations in the BLI effects due to aero-propulsive coupling are less significant when compared to the net BLI effect over a non-BLI vehicle. Thus, while the MDA process is still able to converge to a BLI configuration with a relatively consistent difference in d_2, S, and block fuel, to the equivalent non-BLI configuration, the differences between the coupled and decoupled approaches decreases.

Fig. 16 shows the percentage difference in the block fuel burn estimate between the decoupled (D) and coupled (C) approaches ($100 \times \frac{D-C}{C}$), comparing it between the top and side engine configurations for each case in the FPR and WSR sweeps. The trends observed support the above discussion. The largest difference in the predicted fuel burn between the decoupled and coupled approaches is about 1.7% (628 lbf) for the top-engine configuration at FPR=1.48 for WSR=131.4lbf/ft^2. The fuel burn reduction benefit, comparing the coupled result to the same non-BLI design point is 6.6% (2606 lbf). Thus, the fuel burn discrepancy based on using a decoupled approach instead of a coupled, as a percentage of the fuel burn savings going from non-BLI to BLI ($100 \times \frac{D-C}{\text{No-BLI}-C}$), is about 24% for this design. This difference is a substantial portion of the predicted BLI-benefit and highlights how not modeling the aero-propulsive coupling can be a significant source of uncertainty in the fuel burn savings numbers quoted in literature.

There is some noise in these trends, primarily arising from the the convergence tolerances specified for the multitude of iteration loops involved in this sizing process. There are convergence loops in the MDP engine sizing with the BLI effects, a convergence loop in the aircraft gross weight-wing scaling, and the main vehicle convergence involving scaling of the engine based on the airframe design. While tightening the specified tolerances may flatten some of the observed
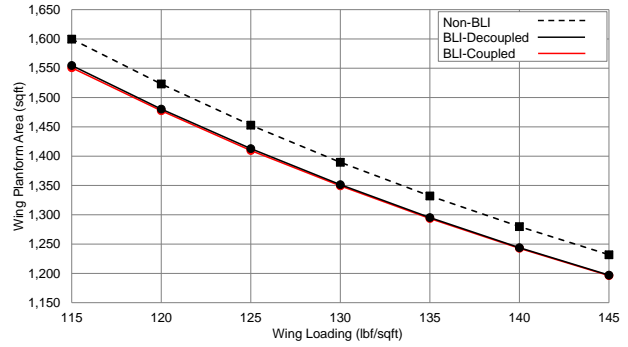
(a) d_2 vs. FPR for WSR=131 lbf/ft^2
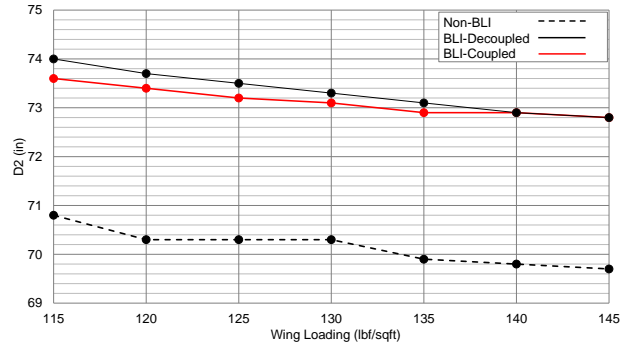
(b) d_2 vs. WSR for FPR = 1.54
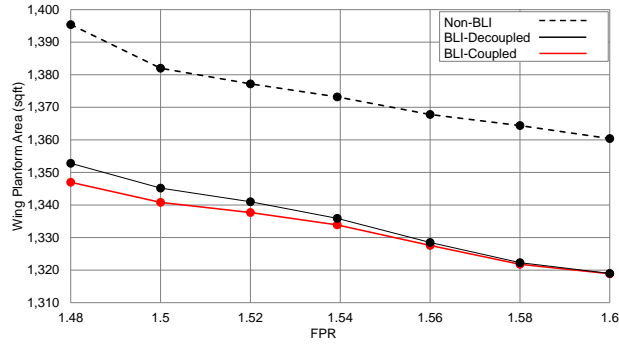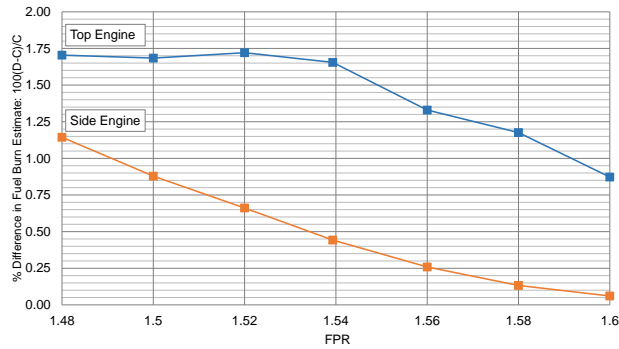
(c) S vs. FPR for WSR=131 lbf/ft^2

(d) S vs. WSR for FPR = 1.54

Fig. 15   Experiment 1: Variations in d_2 and S vs. FPR and WSR for the side engine non-BLI, decoupled-BLI, and coupled-BLI configurations

'bumps', it increases the risk of solver divergence. Minor perturbations to the initial D' values at the engine sizing points helped smoothen out the trends a little, which have been presented in the figures above.

A few comments need to be made to provide some support to the BLI benefit observed relative to the non-BLI configuration. For the top-engine vehicle, in the FPR sweep, there is a fuel burn reduction for the *coupled*-BLI configuration in the range of 5.5% to 6.6% and for the WSR sweep, between 5.6% to 6% relative to the non-BLI aircraft. For the side-engine configuration, the *coupled*-BLI fuel burn reduction varies between 5.2% and 6.1% for the FPR

(a) FPR sweep for WSR=131 lbf/ft^2
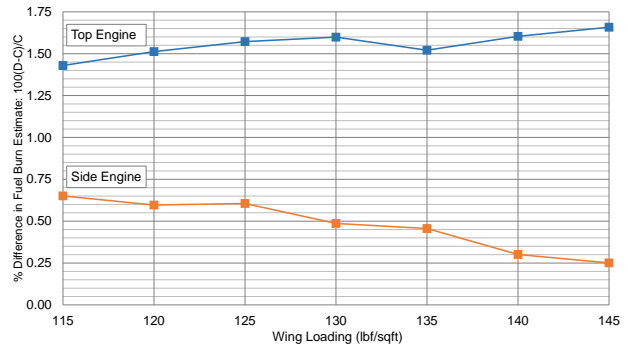
(b) WSR sweep for FPR = 1.54

Fig. 16   Experiment 1: Percentage difference in the block fuel burn estimate between the decoupled and coupled approaches for the top-engine configuration, compared to the side-engine configuration

sweep and between 5.2% to 5.5% for the WSR sweep. *These differences in fuel burn are solely due to BLI and not due to the addition of technologies on the BLI configuration that are not on the non-BLI variants.* While quantifying the BLI benefit relative to a non-BLI configuration is not the primary purpose of this experiment, it should be noted that the fuel burn reductions calculated here are still within expectations. Context can be obtained by looking at some system level BLI studies in literature that have quoted fuel burn reduction numbers. Hardin [51] showed a 3-5% BLI fuel burn benefit for the N+2 BWB concept relative to an appropriate BWB baseline with podded engines. This benefit increased to around 10% for the N+3 BWB concept. Yutko [9] showed a 26-27% block fuel reduction for the D8 compared to the 737-800. Welstead [6] showed a 12% reduction in design block fuel burn for the STARC-ABL, compared to a N3CC non-BLI reference with TRL 6 technologies. In context of the above results, the predicted system level fuel burn savings of 5-7%, using current state of the art technologies for both the BLI and non-BLI variants, is not unrealistic. Sources of uncertainty, in particular the BLI effects prediction errors from the surrogates, can affect these values. This point is discussed further in context of experiment 2.

D. Experiment 1: Sensitivity to Operational Uncertainty in α

To determine whether the assumed h-α schedule affects the conclusions drawn above, α is changed and the FPR sweep is rerun for both the top and side-engine aircraft. The following h-α schedules are investigated:
1) Fixed $\alpha = 3°$ over the entire flight envelope
2) Fixed $\alpha = 1°$ over the entire flight envelope
3) Varied $\alpha = 4°$ for $h < 10,000$ft., $\alpha = 3°$ for $10,000 \leq h < 30,000$ft. and $\alpha = 2°$ for $h \geq 30,000$ft.

Like in Fig. 16a, the percentage difference in block fuel burn benefit between the decoupled and coupled approaches is tracked and compared between engine locations, for the different schedules. Fig. 17 presents these trends. Trends from Fig. 16a are also included for reference. As expected, there are variations in the trends, highlighting an additional source of uncertainty in fuel burn savings from BLI. However, the top-engine configuration consistently shows appreciable differences between the two approaches, and these differences are larger than those for the side-engine configuration. Thus, regardless of the h-α schedule assumed, aero-propulsive interactions due to BLI must be captured as part of the design methodology. For experiment 2, the original h-α map is used.
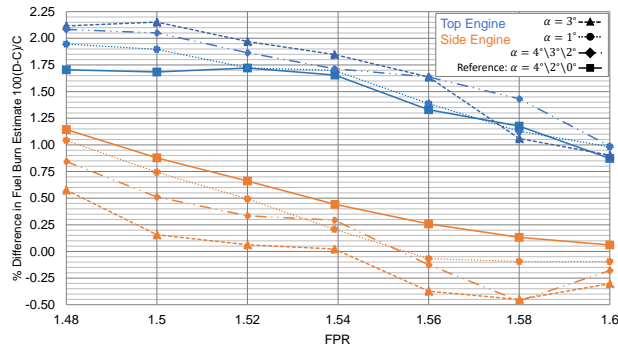
Fig. 17   Experiment 1: Percentage difference in the block fuel burn estimate between the decoupled and coupled approaches for the top-engine configuration, compared to the side-engine configuration, for varying h-α maps

VI. Vehicle Optimization and Experiment 2

An extended design space exploration study is conducted and the optimum vehicle designs are chosen, first based on lowest block fuel burn, and then smallest TOGW. The design space exploration and optimization serve two purposes:
1) Extend experiment 1 by looking at more airframe and cycle design parameters to investigate differences in trends of key metrics when comparing the decoupled approach to the coupled approach for both engine locations
2) Determine whether the optimized designs differ between the two approaches and how these differences compare between the top and side engine aircraft

Differences in the trends and optimized designs lend further support to the need for a coupled and parametric aero-propulsive methodology for BLI concept design. Given that the vehicle sizing loop in EDS takes only a few minutes to run, several hundreds of cases can be run *in parallel* for different design combinations in a design space exploration

study. Main design and performance metrics for each case can be recorded and surrogate models can be generated for each response. With the surrogates, one gets a visual comparison of the trends, and one can also optimize on these surrogates. The design space exploration and optimization process is described in the following sub-section.

A. Experiment 2: Design Space Exploration and Optimization

The design space exploration and optimization are conducted for both the non-BLI and BLI variants of the top-engine and side-engine configurations. For the BLI versions, two separate studies are conducted: one with BLI-coupling, and the other decoupled. The design variables considered are shown in Table 5. An OPR constraint in the range of 45-55 (assuming duct losses) is imposed based on expected values for a direct drive fan in the 2035 time frame. This constraint filters out infeasible combinations of FPR, LPCPR, and HPCPR within the specified bounds. A leading edge sweep constraint between 20°-40° is also imposed. FLOPS internal aerodynamics are based on quarter chord sweep. The BLI surrogates, however, were modeled using leading edge sweep. Since the mapping between quarter chord and leading edge sweep is based on taper ratio and aspect ratio, the leading edge sweep constraint filters out disallowed combinations of AR, λ, and $\Lambda_{c/4}$. The ramp angle variable does not feature in the non-BLI design space exploration.

Table 5   Experiment 2: Design Variables for Design Space Exploration

Input Variable	LB	UB	Type	Comments
FPR	1.48	1.60	Propulsor	OPR Constraint 45-55
LPCPR	1.25	2.25	Propulsor	OPR Constraint 45-55
HPCPR	15	35	Propulsor	OPR Constraint 45-55
AR	7	11	Airframe	
λ	0.2	0.4	Airframe	
$\Lambda_{c/4}$ (°)	20	40	Airframe	Λ_{LE} constraint 20°-40°
ϕ (°)	12	20	Airframe	Only for BLI variants
WSR	115	145	Airframe	

Two space filling DoEs are created in JMP for the non-BLI and BLI studies. Each DoE has 2000 cases that are split 75%-25% for training and validation. There are enough cases within each DoE to account for significant non-linearity in the responses and failed cases due to convergence issues. The metrics of interest are design block fuel, d_2, S, TOFL, LDGFL, TOGW, and SLS thrust per engine. An artificial neural network model is used to fit these reposes, with the
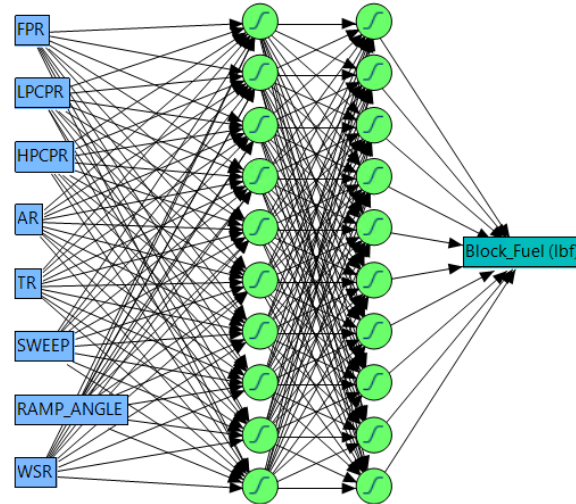

Fig. 18   Example of ANN architecture used to fit a surrogate model to EDS responses, in this case block fuel. The ramp angle input is omitted for non-BLI cases

final architecture shown in Fig. 18. The number of neurons per layer and number of hidden layers are determined based on the surrogate model diagnostic measures for each response, introduced in context of the BLI effects models in section IV.B. The final surrogate model quality metrics are calculated automatically by JMP for the non-BLI, BLI-coupled, and BLI-decoupled variants. Failed cases and some outliers are excluded. Responses have an R^2 value above 0.99 for both training and validation. The actual vs. predicted and residual vs. predicted plots are indicative of good fits, based on criteria described previously. The MFE and MRE distributions have a mean error close to 0% along with a standard deviation and max error range well within 1%. Based on this diagnostic information, the surrogates of the system level metrics are excellent. The exception is TOFL, which compared to the other responses, shows the weakest fit. The prediction errors for this response do not always satisfy the same error tolerances as the other responses. This relatively poorer fit is not a major concern given that TOFL is merely used as a constraint within the optimization problem. The optimized design performance is verified with EDS to ensure that all constraints are satisfied.

The design space can be viewed through a series of profiler plots generated by JMP. The neural network models behind these trends form a fully parametric environment, where the design point can be easily changed to observe corresponding changes to the system level responses. These profilers are shown at the baseline design point in Table 1, for the non-BLI top-engine configuration in Fig. 19 and for the side-engine configuration in Fig. 20. It should be noted that the trends observed in these figures can change depending on the design value picked, based on interactions between variables. As such, the plots are merely meant to provide a general overview of the design space at a given design point. The trends for both the top and side-engine aircraft are similar, as expected. To minimize fuel burn, the trends suggest higher pressure ratios and aspect ratio as expected. A lower taper ratio is desirable to maintain an elliptical lift distribution, while interestingly, smaller sweep angles also appear to minimize fuel burn. For a transonic aircraft,
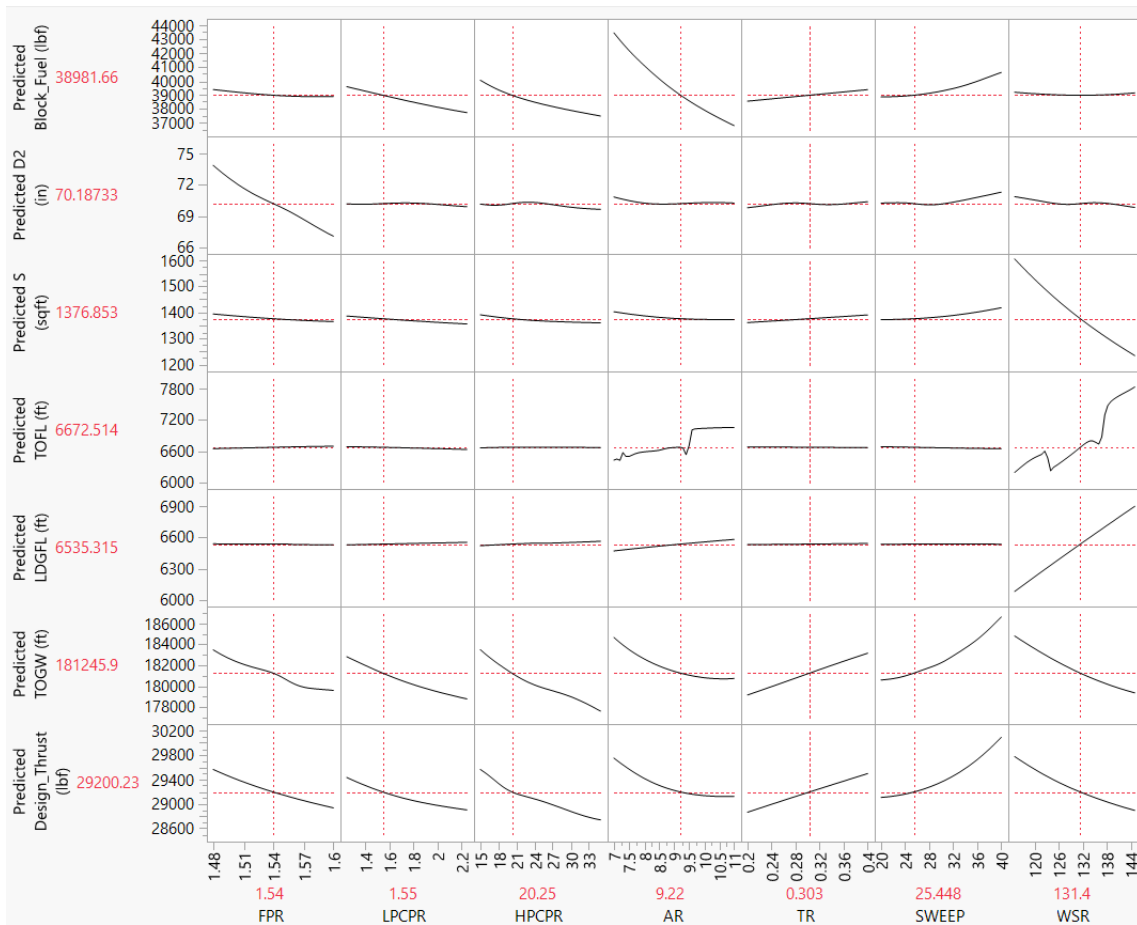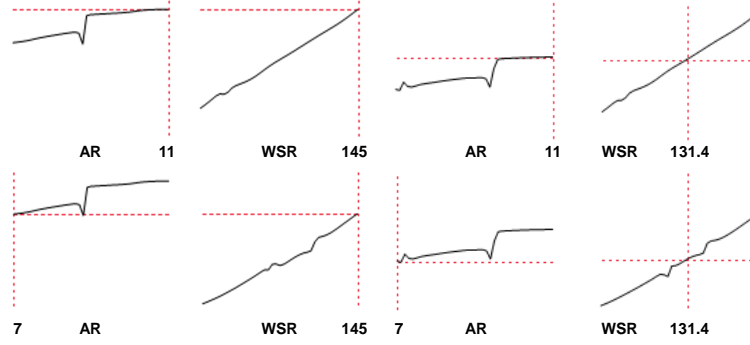

Fig. 19   Experiment 2: Top-Engine Non-BLI profiler plots showing trends of key metrics with the design variables at the design point shown in Table 1
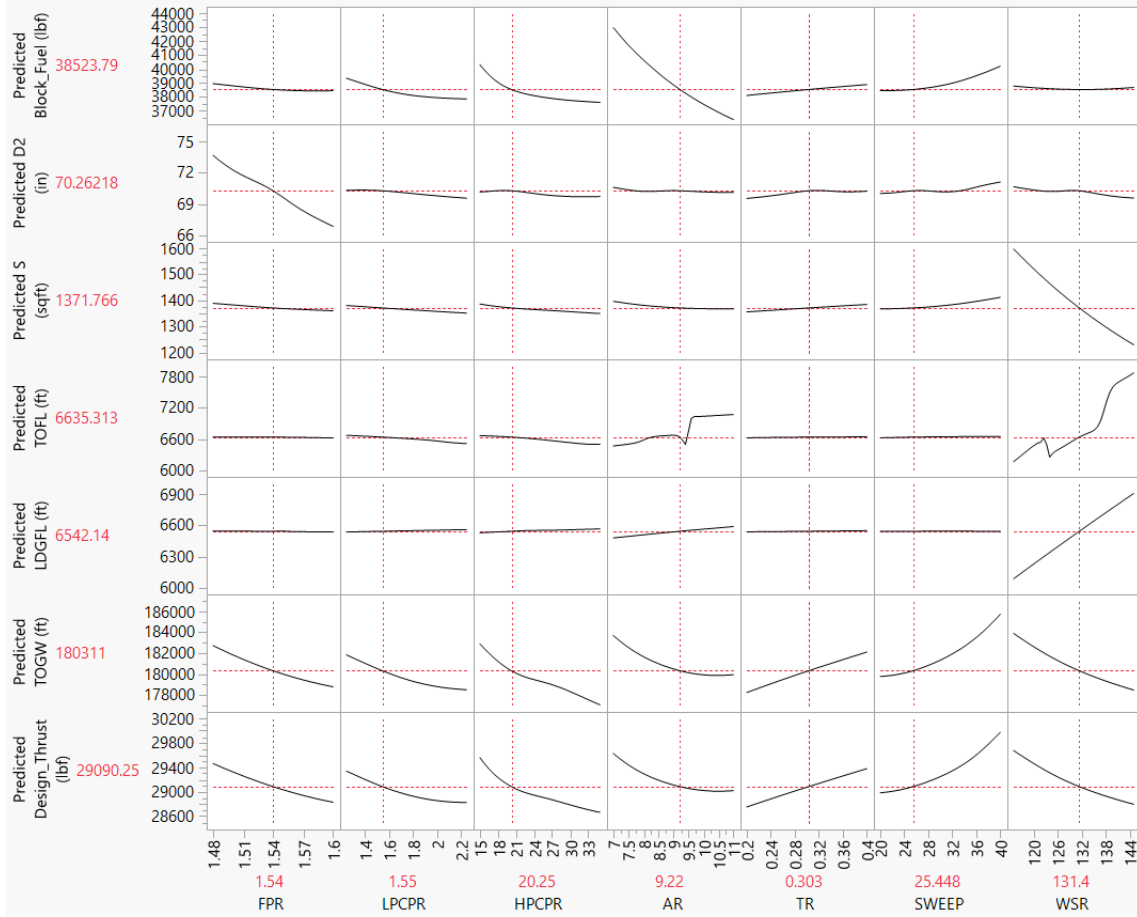
Fig. 20 Experiment 2: Side-Engine Non-BLI profiler plots showing trends of key metrics with the design variables at the design point shown in Table 1

increasing sweep decreases drag, but also lowers lift. Depending on the operating weight of the vehicle and the required lift at a given flight condition, increasing sweep may not be optimal. In addition, for a given wing span, increasing sweep increases the length of the wing spars and their required stiffness must also increase. Consequently, wing weight increases with sweep, which has an adverse impact on required block fuel. Lastly, the wing loading trend shows a bucket, implying an optimum somewhere in the middle of the specified range. The block fuel, d_2 and S variations with FPR and WSR are consistent with the trends shown in experiment 1.1 for the non-BLI aircraft. TOGW trends are also expected, with a reduction in TOGW observed with FPR, LPCPR and HPCPR, which is mostly driven by the fuel burn benefits of a higher OPR. While higher aspect ratio wings are expected to be heavier, it would appear that the aerodynamic benefit of such wings and their subsequent impact on fuel burn savings is the dominant factor. TOGW trends with taper and wing sweep are driven by both the aerodynamic impacts of these variables on fuel burn, discussed previously, and by the wing weight penalties incurred by increasing these values.

The reader may also notice a strange trend of TOFL with aspect ratio and wing loading for both configurations. Focusing on the general direction of the trends first, at the design point shown in the figures above, an increase in TOFL with an increase in aspect ratio and wing loading is observed. TOFL also shows greater sensitivity to WSR. The smaller wing, as a consequence of higher wing loading, severely penalizes its lifting capability, explaining the increase in TOFL. For a given wing loading, an increase in AR has a favorable impact on fuel burn and thus results in a decrease in TOGW. To maintain the same WSR, the wing planform area must decrease. As such, takeoff performance is penalized, albeit not to the same degree as that from an increase in WSR. The neural network models also pick up an interaction effect between these two variables that alters the shape of these trends, as shown for the top-engine non-BLI configuration in Fig. 21 for example. Notice how the TOFL trends vs. wing loading are now linear with a positive slope, as one would expect.

Fig. 21 Experiment 2: Top-Engine non-BLI TOFL trends with AR and WSR showing interaction effects between the variables

The non-smooth trends of TOFL vs. AR and WSR suggests numerical issues, rather than physics based phenomena. Possible explanations include noise in the responses used to train the surrogate, impact of outliers, and model over fitting to noisy data. From the actual vs. predicted, residual vs. predicted, MFE and MRE plots, several points were observed to be outliers for the TOFL responses that were not so for any of the other metrics. These issues, however, are ultimately not a major concern for experiment 2, as explained above. As a preview, for the optimized designs shown in Table 6, the final TOFL values are far away from the specified constraint for the model to bias the outcome. For the optimized designs in Table 7, the EDS predictions and surrogate predictions for TOFL agree well.
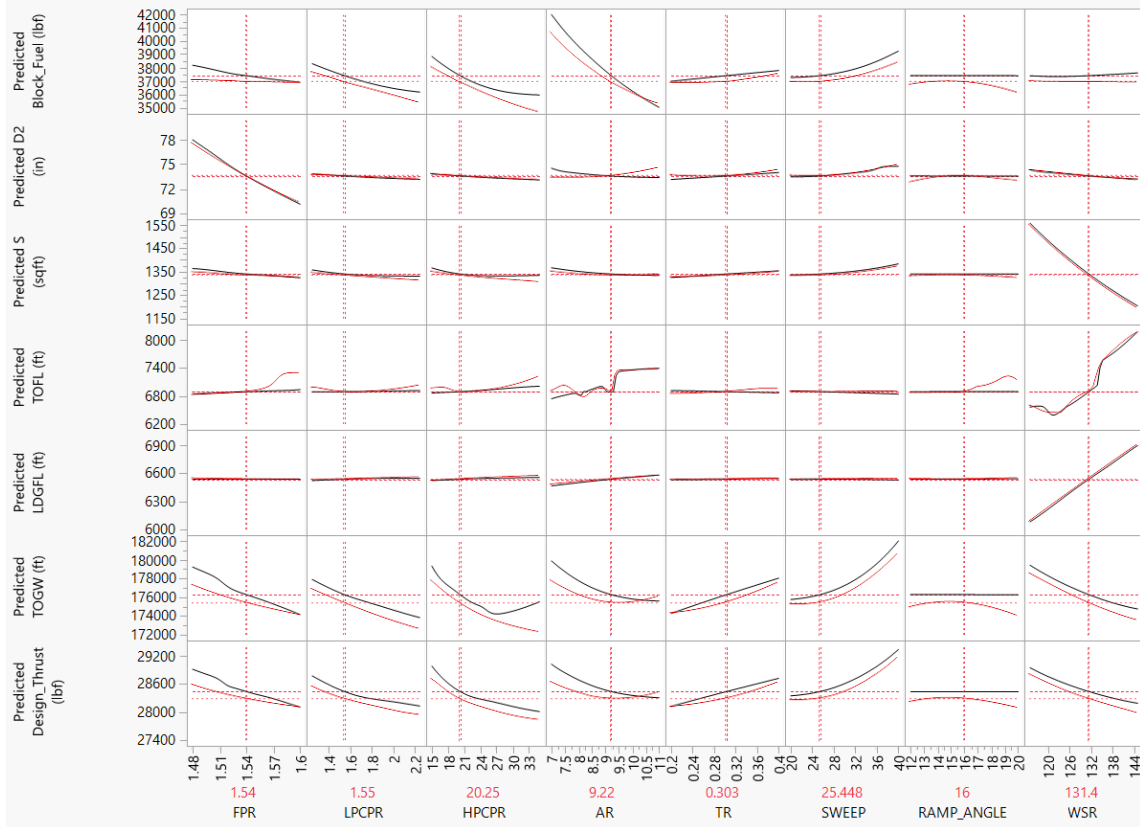
Fig. 22 Experiment 2: Top-Engine BLI profiler plots showing trends of key metrics with the design variables at the design point shown in Table 1. The coupled approach trends are shown in red and the decoupled in black
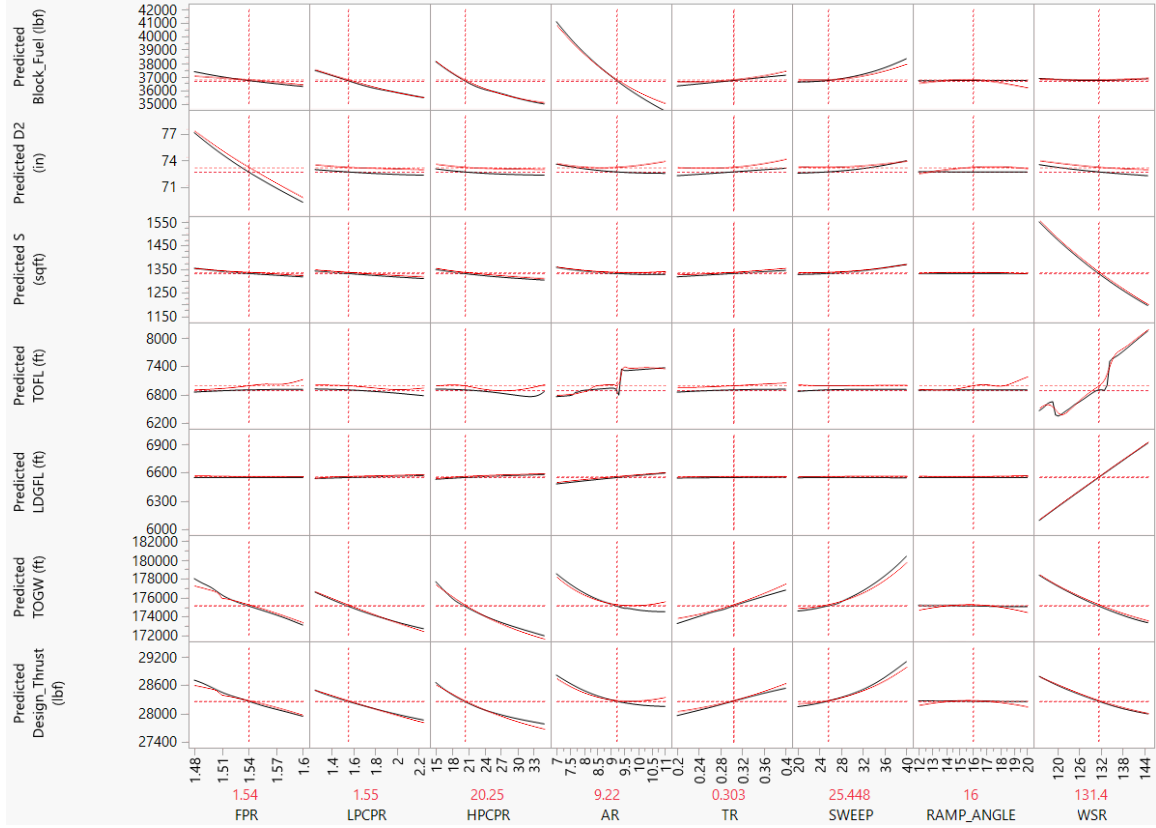
Fig. 23   Experiment 2: Side-Engine BLI profiler plots showing trends of key metrics with the design variables at the design point shown in Table 1. The coupled approach trends are shown in red and the decoupled in black

The non-BLI responses are only intended to provide a reference to the observed BLI-results and a set of inputs to the BLI surrogates for the decoupled approach. The main focus is on the differences in the BLI responses, for a given engine location, between the decoupled and coupled approaches. Fig. 22 compares the decoupled and coupled trends for the top-engine configuration, while Fig. 23 does the same for the side-engine vehicle. Both the decoupled and coupled trends in general are similar to the non-BLI counterparts. The 'anomalies' in TOFL trends with AR and WSR also persist for the BLI concepts, despite the remaining responses showing smooth behavior. Recall, the decoupled approaches in literature use a fixed aircraft geometry to obtain estimates of the BLI effects. For these decoupled trends, inputs to the BLI effects surrogates are fixed at the non-BLI optimized values, summarized in Table 6. Consistent with experiment 1, there are noticeable differences between the decoupled and coupled trends for the top-engine configuration, which are much smaller for the side-engine aircraft. There is also agreement between the surrogate model trends for block fuel, d_2, and S with FPR and WSR, and the EDS results in experiment 1. Despite variations in the decoupled and coupled trends, expected optimum design variable values for minimum fuel burn do not appear to be significantly different at first glance.

Optimization of the BLI and non-BLI aircraft is conducted in JMP with the help of desirability functions [52]. The design block fuel is defined as the objective function. The following constraints are imposed on the optimization problem, implemented using disallowed combinations and desirability functions in JMP:

1) $45 \leq$ OPR ≤ 55 with assumed pressure ratio multiplier of 0.985 to account for duct losses between the compressors
2) $20° \leq \Lambda_{LE} \leq 40°$ since inputs for FLOPS require quarter chord sweep and inputs to the BLI surrogates are based on leading edge sweep
3) $68in \leq d_2 \leq 78in$
4) TOFL (All Engine Operational) $\leq 8000ft$
5) LDGFL $\leq 8000ft$

28

The objective function is optimized ten times with different initial values and the resulting designs that meet the constraints with the lowest fuel burn are recorded. Each of these designs are then run through EDS to verify the results predicted by the surrogates, and then the best designs are chosen. The final designs are compared in Table 6. The predicted BLI fuel burn reduction, comparing the coupled-BLI to the non-BLI optimum is 6.2% for the top-engine and 6.5% for the side-engine vehicles. The two modeling approaches show different optimum values of HPCPR, LPCPR, and quarter chord sweep. Other variables are the same. All optimized BLI vehicles favor smaller engines, based on the optimum FPR of 1.6. It would appear that the aerodynamic penalty on D' due to larger fans is more substantial than the propulsive efficiency benefit, even for BLI, hence the trend towards higher FPR fans. The higher FPR fan for BLI variants, compared to non-BLI, suggests that the propulsive efficiency loss going to a smaller fan is offset by the BLI benefit. Optimum values for OPR, AR, and λ are all expected, the latter two primarily driven by the aerodynamic impacts on D'. The optimum value of inlet ramp angle being at the lower bound is indicative of the competing effects of η_{PR} and $P_{K_{in}}$, $\Delta\Phi_{wake}$. Experiment 8 in [33] showed that both $P_{K_{in}}$ and $\Delta\Phi_{wake}$ increased with ramp angle, but η_{PR} decreased. In Fig. 22 for example, $\phi = 12°$ and $\phi = 20°$ show the lowest fuel burn for the selected design point, with the latter being the global optimum. Increasing block fuel burn with an increase in the ramp angle from $12°$ suggests that the η_{PR} losses are more dominant, but after a certain value, the $P_{K_{in}}$ and $\Delta\Phi_{wake}$ benefits overcome the η_{PR} losses. Due to interactions with the wing, at the optimum design, this trend changes and $12°$ results in lower fuel burn.

The same exercise is repeated with TOGW as the objective function instead. A comparison of the optimum designs is presented in Table 7. In this design space, lower TOGW is primarily achieved through a reduction in the wing weight. This is possible with a smaller wing planform and a lower quarter chord sweep. The smaller wing, however, comes at the cost of an increase in block fuel burn, takeoff length, and landing field length. Differences between the coupled and decoupled designs are again primarily seen in HPCPR, LPCPR, and quarter chord sweep, along with a small difference in AR for the top-engine configuration. This difference in AR results in a larger block fuel and TOGW discrepancy between coupled and decoupled (-2.41% and -0.19% respectively) for the TOGW optimized top-engine configuration, when compared to the fuel optimized vehicle (0.13% for fuel and 0.04% for TOGW), where the optimum AR is the same for both decoupled and coupled. Also, since TOGW accounts for both OEW and fuel weight, by ignoring sizing impacts on the BLI effects, the error observed in both metrics can be exaggerated when one aims to minimize TOGW.

Table 6   Experiment 2: Comparison of Block Fuel Optimized Designs

	Top-Engine			Side-Engine		
Design Var.	Non-BLI	BLI-C	BLI-D	Non-BLI	BLI-C	BLI-D
FPR	1.566	1.6	1.6	1.553	1.6	1.6
LPCPR	2.007	1.659	1.263	1.841	1.341	1.482
HPCPR	17.748	21.028	27.628	19.525	26.018	23.537
AR	11	11	11	11	11	11
λ	0.2	0.2	0.2	0.2	0.2	0.2
$\Lambda_{c/4}$ (°)	24	27.62	24	24	28.41	24
WSR	130	130	130	133.5	130	130
ϕ (°)	NA	12	12	NA	12	12
Key Outputs						
Des. Block Fuel (lbf)	35824	33619	33663	35491	33198	33272
S (ft^2)	1357	1313	1314	1319	1312	1308
d_2 (in)	68	69.3	69.5	68.4	68.8	68.8
OPR	55	55	55	55	55	55
TOGW (lbf)	176429	170726	170801	176082	170513	170023
AEO TOFL (ft)	6988	7393	7403	7208	7374	7386
LDGFL (ft)	6535	6550	6553	6641	6562	6556

29

Table 7 Experiment 2: Comparison of TOGW Optimized Designs

Design Var.	Top-Engine Non-BLI	Top-Engine BLI-C	Top-Engine BLI-D	Side-Engine Non-BLI	Side-Engine BLI-C	Side-Engine BLI-D
FPR	1.558	1.599	1.6	1.546	1.592	1.6
LPCPR	1.354	1.396	1.282	1.841	1.616	1.849
HPCPR	26.469	25	27.215	19.619	21.524	18.876
AR	11	10.24	11	11	11	11
λ	0.2	0.2	0.2	0.2	0.2	0.2
$\Lambda_{c/4}$ (°)	20	24	20	20	24	20
WSR	145	137	136	145	136	136
ϕ (°)	NA	12	12	NA	12	12
Key Outputs						
Des. Block Fuel (lbf)	36029	34576	33742	35651	33266	33325
S (ft^2)	1206	1242	1253	1203	1246	1241
d_2 (in)	68.1	69.2	69.2	68.5	69	68.5
OPR	55	55	55	55	55	55
TOGW (lbf)	174856	170144	169814	174497	169113	168789
AEO TOFL (ft)	7972	7805	7732	7952	7734	7739
LDGFL (ft)	6942	6721	6699	6950	6712	6717

B. Comments on BLI Effects Surrogate Model Prediction Error

All results generated so far depend on the accuracy of the BLI effects surrogate models in capturing the 'true' response, as would be predicted by CFD. However, each of the surrogates shows a certain distribution on prediction error, that is highlighted in the MFE and MRE distributions for a given response. While the main objective of this study was to quantify the uncertainty in the predicted BLI fuel burn savings as a result of ignoring aero-propulsive coupling, it is also worthwhile to estimate uncertainty in the predicted BLI fuel burn savings as a result of surrogate prediction error. Specifically, an estimate for the theoretical upper and lower bound on fuel burn, based on the largest prediction errors for each surrogate, will provide a perspective on the potential variability of the response. The TOGW optimized (coupled approach) top-engine configuration shown in Table 7 is used as a test case for this quick study.

For each BLI surrogate, prediction errors at the 2.5 and 97.5 percentiles are recorded for the combined training and validation dataset. Thus, 95% of the data is covered with this range. Additionally, the test case geometry is run in CFD at the start and end cruise points, which are at $M_\infty = 0.78$ at 35,000 ft. and 39,000 ft. The BLI effects calculated in CFD are compared against the surrogate predictions. Thus, a CFD generated cruise point error estimate for each BLI effect is also obtained. To get the largest and smallest fuel burn estimate, the upper and lower percentile errors need to be combined in a logical manner, while accounting for the physics. In general, $P_{K_{in}}$ and $\Delta\Phi_{wake}$ correlate opposite to η_{PR}, as seen in the [33]. So for example, setting the percentage errors at the largest positive value for the first two BLI effects requires that the η_{PR} error be set to the largest magnitude negative value.

An interesting finding is that within these error ranges, fuel burn is more sensitive to errors in η_{PR} than the combined effect of errors in $P_{K_{in}}$ and $\Delta\Phi_{wake}$. Thus, to estimate the upper bound on fuel burn, the percentage error for η_{PR} should be set to the largest magnitude negative value. The three trials conducted to get the fuel burn error estimates are shown in Table 8. The cruise error point is defined by the average of the percentage error at the start and end points. It should be noted that the percentage errors shown for the three CFD measured BLI effects apply to the transformed metrics that were used as the surrogate responses. For each trial, the percentage error in the response is applied as a correction to the BLI effects surrogates within EDS, at every operating point, and the fuel burn from the resulting design is tracked. This approach assumes that the same percentage error for a BLI response is valid across the entire mission. This assumption is not quite true, as evident in the percent error variation between the start and end of cruise. This assumption however does simplify the process and allow for a quick estimation of the fuel burn range, which is adequate for now.

Table 8 Summary of Model Prediction Percentage Errors

Condition	$P_{K_{\text{in}}}$	η_{PR}	$\Delta\Phi_{\text{wake}}$	SWETF	SWETN
1) Fuel Burn Upper Bound	1.81	-1.51	2.89	0.0013	0.0028
2) Fuel Burn Lower Bound	-1.54	1.32	-3.29	-0.0020	-0.0050
Start of Cruise	1.37	-0.62	0.61	0	0
End of Cruise	1.31	-0.20	0.32	0	0
3) Cruise Average	1.34	-0.41	0.46	0	0

Fig. 24 presents the results from this study. In Fig. 24a, ranges on block fuel are shown for the coupled TOGW optimized design in red. The value of fuel burn predicted by EDS (as shown in Table 7) without any error correction on the BLI surrogates is shown as a red circle. The fuel burn prediction upon applying the errors calculated through the CFD spot check at cruise is shown with a red cross. The fuel burn ranges for the corresponding decoupled TOGW optimized top-engine design are also shown for reference purposes. Since the CFD cruise error point was obtained from the coupled optimum geometry, it cannot be applied to the decoupled design results and is thus not shown for this case. The TOGW optimized non-BLI design fuel burn (also shown in Table 7), is included for comparison. Ranges on the BLI fuel burn percent savings going from the optimized non-BLI to the optimized BLI designs are presented in a similar format in Fig. 24b. The following conclusions can be drawn from these figures:

1) The upper and lower error bound in the BLI fuel burn savings is on the same order of magnitude as the predicted BLI fuel burn savings
2) This discrepancy, however, is one order of magnitude smaller than the predicted BLI fuel burn savings, using the more realistic cruise point surrogate error
3) Differences in fuel burn between the decoupled and coupled designs is maintained at the upper and lower error bounds as well

The large range in fuel burn error and thus the predicted BLI fuel burn savings clearly motivates the need for a formal uncertainty quantification study. This study will help paint a more realistic picture by providing a distribution of fuel burn, based on assumed surrogate error distributions, rather than just the worst case upper and lower bounds. From this distribution, one can determine the probability of encountering a given fuel burn value within the ranges shown in Fig. 24, thereby providing better context concerning the accuracy of the BLI effects surrogates. With respect to the cruise error spot check, given that this regime constitutes a major part of the mission, surrogate prediction errors calculated here through CFD provide a more representative estimate of the actual fuel burn error for a given design. The small magnitude of fuel burn discrepancy, resulting from the CFD spot check of surrogate error, is thus quite encouraging. This result lends confidence to the optimized designs and the conclusions drawn in this paper.

(a) Block fuel burn (lbf)

(b) BLI fuel burn percent savings
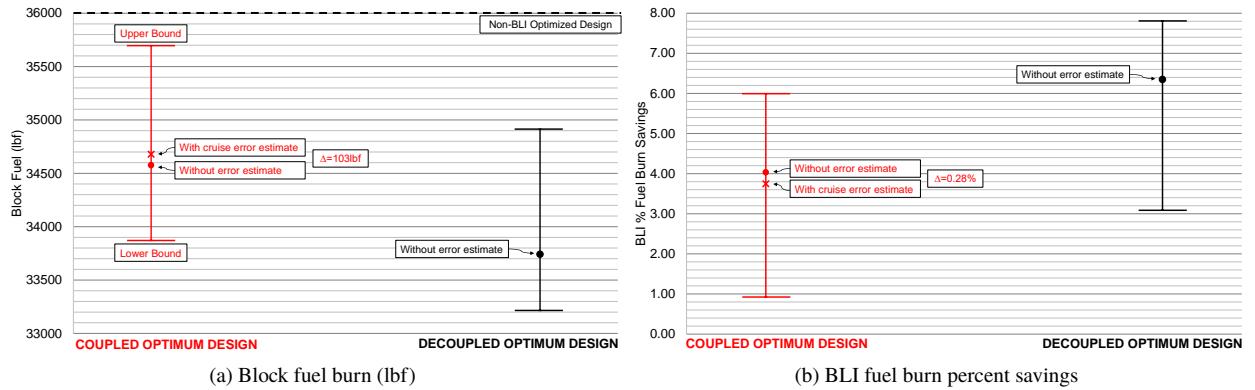
Fig. 24 Error ranges in block fuel and BLI fuel savings for the top-engine TOGW optimized configurations, relative to the top-engine non-BLI optimized design

VII. Concluding Remarks

Experiments 1 and 2 clearly show the scope of potential uncertainty in BLI aircraft design and performance by using a decoupled approach instead of a coupled. As observed in experiment 1 for example, the discrepancy in fuel burn introduced by using a fixed point design estimate (decoupled approach) for the BLI effects, instead of a parametric and coupled estimation, can be anywhere in the range of 0.06% to 1.7%, depending on the aircraft design and engine location. For the designs considered in experiment 1, the fuel burn savings relative to the non-BLI configuration is between 5-7%. As a fraction of the predicted BLI fuel burn savings relative to the non-BLI configuration, the error due to ignoring aero-propulsive coupling can be as high as 24%. Experiment 2 showed noticeable differences in optimized engine cycle and airframe design as a result of ignoring aero-propulsive coupling.

A caveat to the results in this paper concerns the role of uncertainty in the value of the BLI effects. For example, the operational uncertainty study in experiment 1 (Fig. 17) regarding the assumed angle of attack variations over the mission showed how the fuel burn predictions changed based on the angle of attack assumptions. A consequence of this uncertainty is the discrepancy between the decoupled and coupled fuel burn predictions, which in general was higher than the numbers stated above. The impact of surrogate prediction error on the BLI fuel burn savings was also highlighted in a quick study discussed in section VI.B. The 5-7% fuel burn savings stated above is thus subject to a certain degree of variation, depending on the significance of the surrogate prediction errors. Distortion impacts, if modeled, are also expected to affect this range.

While the BLI effects modeled in this study are defined based on Drela's power balance, which in turn is derived from the conservation laws, calculation of these quantities in CFD is an exercise that requires a certain degree of engineering judgment. As a consequence, there is also some uncertainty in the BLI effects estimates due to implementation differences. As discussed before, common to both $P_{K_{\mathrm{in}}}$ and $\Delta\Phi_{\mathrm{wake}}$ is the problem of defining the control volume boundaries on which these terms are to be integrated. The other source of uncertainty arises from the physical model used to estimate the wake dissipation change due to BLI.The conclusions drawn in this study are based on differences in performance and design between coupled and decoupled approaches. These conclusions should be valid regardless of the implementation uncertainty, since the same modeling technique is used for all experiments. However, since the BLI effects, and thus the fuel burn estimate for the BLI configuration, are subject to this uncertainty, it is worthwhile to look into the following aspects: i) whether this implementation uncertainty matters? and ii) if so, is there a basis to strongly favor one approach over the other? The first question can be addressed by repeating the experiments 1 and 2 in this study, using different combinations of the above modeling approaches when generating the surrogates. Sensitivity of the performance and design of the BLI vehicle to these implementation differences determines the need to address question (ii). This question can potentially be answered by comparing the fuel burn estimates from power balance to a study that calculates fuel burn from the net axial force F_X on the aircraft.

Despite these acknowledged sources of uncertainty that arise from pragmatic implementation methods, the trends show strong support for use of coupled and parametric methodologies for BLI concept design. The proposed method thus serves as a foundation for future BLI concept design studies.

References

[1] Suder, K., "Overview of the NASA Environmentally Responsible Aviation Project's Propulsion Technology Portfolio," *48th AIAA/ASME/SAE/ASEE Joint Propulsion Conference & Exhibit, Joint Propulsion Conferences*, AIAA, 2012. https://doi.org/10.2514/6.2012-4038.

[2] Muller, R., "ACARE Goals (AGAPE) Progress Evaluation, Project Final Report Publishable Summary," Report, Advisory Council for Aeronautics Research in Europe, 2010.

[3] Betz, A., *Introduction to the Theory of Flow Mechanics*, 1$^{\mathrm{st}}$ ed., Pergamon Press, Karlsruhe, Germany, 1966.

[4] Felder, J. L., Kim, H. D., and Brown, G. V., "Turboelectric Distributed Propulsion Engine Cycle Analysis for Hybrid-Wing-Body Aircraft," *47th AIAA Aerospace Sciences Meeting including the New Horizons Forum and Aerospace Exposition*, AIAA, 2009. https://doi.org/10.2514/6.2009-1132.

[5] Felder, J. L., Kim, H. D., Brown, G. V., and Chu, J., "An Examination of the Effect of Boundary Layer Ingestion on Turboelectric Distributed Propulsion Systems," *49th AIAA Aerospace Sciences Meeting including the New Horizons Forum and Aerospace Exposition*, AIAA, 2011. https://doi.org/https://doi.org/10.2514/6.2011-300.

[6] Welstead, J. R., and Felder, J. L., "Conceptual Design of a Single-Aisle Turboelectric Commercial Transport with Fuselage Boundary Layer Ingestion," *AIAA SciTech Forum*, AIAA, 2016. https://doi.org/10.2514/6.2016-1027.

[7]   Greitzer, E. M., Bonnefoy, P. A., De la Rosa Blanco, E., Dorbian, C., Drela, M., and Hall, D. K., "N+3 Aircraft Concept Designs and Trade Studies, Final Report," Report, NASA Glenn Research Centre, 2010.

[8]   Drela, M., "Development of the D8 Transport Configuration," *AIAA Applied Aerodynamics Conference*, AIAA, 2011.

[9]   Yutko, B., Titchener, N. A., Courtin, C., Lieu, M. K., Wirsing, L., Tylko, J., Chambers, J., Roberts, T., and Clint, C., "Conceptual Design of a D8 Commercial Aircraft," *AIAA Aviation Forum*, AIAA, 2017.

[10]   Wiart, L., Atinault, O., Grenon, R., Paluch, B., and Hue, D., "Development of NOVA Aircraft Configurations for Large Engine Integration Studies," *33rd AIAA Applied Aerodynamics Conference*, AIAA, 2015.

[11]   Ahuja, J., "A Methodology for Capturing the Aero-Propulsive Coupling Characteristics of Boundary Layer Ingesting Aircraft in Conceptual Design," Thesis, 2020.

[12]   Liebeck, R. H., Page, M. A., and Rawdon, B. K., "Blended-Wing-Body Subsonic Commercial Transport," *36th AIAA Aerospace Sciences Meeting and Exhibit*, AIAA, 1998.

[13]   Liebeck, R. H., "Blended Wing Body Design Challenges," *AIAA International Air and Space Symposium and Exposition: The Next 100 Years*, AIAA, 2003. https://doi.org/10.2514/6.2003-2659.

[14]   Liebeck, R. H., "Design of the BlendedWing Body Subsonic Transport," *Journal of Aircraft*, Vol. 41, No. 1, 2004. https://doi.org/10.2514/1.9084.

[15]   Hendricks, E., "A Review of Boundary Layer Ingesting Modeling Approaches for use in Conceptual Design," Report, NASA Glenn Research Center, 2018.

[16]   Hileman, J., Spakovszky, Z., Drela, M., and Sargeant, M. A., "Aerodynamic and Aeroacoustic Three-Dimensional Design for a "Silent" Aircraft," *44th AIAA Aerospace Sciences Meeting and Exhibit*, AIAA, 2006.

[17]   Hileman, J. I., Spakovszky, Z. S., and Drela, M., "Airframe Design for "Silent Aircraft"," *45th AIAA Aerospace Sciences Meeting and Exhibit*, AIAA, 2007. https://doi.org/10.2514/6.2007-453.

[18]   Hall, C. A., and Crichton, D., "Engine Design Studies for a Silent Aircraft," *Journal of Turbomachinery*, Vol. 129, No. 3, 2006, p. 9. https://doi.org/10.1115/1.2472398.

[19]   Plas, A. P., Sargeant, M. A., Madani, V., Crichton, D., and Greitzer, E. M., "Performance of a Boundary Layer Ingesting (BLI) Propulsion System," *45th AIAA Aerospace Sciences Meeting and Exhibit*, AIAA, 2007.

[20]   Kuntawala, N. B., Hicken, J. E., and Zingg, D. W., "Preliminary Aerodynamic Shape Optimization of a Blended-Wing-Body Aircraft Configuration," *49th AIAA Aerospace Sciences Meeting including the New Horizons Forum and Aerospace Exposition*, AIAA, 2011. https://doi.org/10.2514/6.2011-642.

[21]   Reist, T. A., and Zingg, D. W., "Aerodynamic Shape Optimization of a Blended-Wing-Body Regional Transport for a Short Range Mission," *31st AIAA Applied Aerodynamics Conference*, AIAA, 2013. https://doi.org/10.2514/6.2013-2414.

[22]   Lyu, Z., and Martins, J. R. R. A., "Aerodynamic Design Optimization Studies of a Blended-Wing-Body Aircraft," *Journal of Aircraft*, Vol. 51, No. 5, 2014. https://doi.org/10.2514/1.C032491.

[23]   Gray, J. S., Mader, C. A., Kenway, G. K., and Martins, J. R. R. A., "Modeling Boundary Layer Ingestion Using a Coupled Aeropropulsive Analysis," *Journal of Aircraft*, Vol. 55, No. 3, 2018. https://doi.org/10.2514/1.C034601.

[24]   Gray, J. S., and Martins, J. R. R. A., "Coupled Aeropropulsive Design Optimization of a Boundary Layer Ingestion Propulsor," *The Aeronautical Journal*, 2018, p. 19.

[25]   Ordaz, I., Rallabhandi, S., Nielsen, E. J., and Diskin, B., "Mitigation of Engine Inlet Distortion through Adjoint-Based Design," *AIAA AVIATION Forum*, AIAA, 2017.

[26]   Rodriguez, D. L., "Multidisciplinary Optimization Method for Designing Boundary-Layer-Ingesting Inlets," *Journal of Aircraft*, Vol. 46, No. 3, 2009. https://doi.org/10.2514/1.38755.

[27]   Gray, J. S., Kenway, G. K., Mader, C. A., and Martins, J. R. R. A., "Aeropropulsive Design Optimization of a Turboelectric Boundary Layer Ingestion Propulsion System," *Aviation 2018*, AIAA, 2018. https://doi.org/10.2514/6.2018-3976.

[28]   Kim, H., and Liou, M.-S., "Optimal Shape Design of Mail-Slot Nacelle on N3–X Hybrid Wing-Body Configuration," *31st AIAA Applied Aerodynamics Conference*, AIAA, 2013. https://doi.org/10.2514/6.2013-2413.

[29] Kim, H., and Liou, M.-S., "Optimal Inlet Shape Design of N2B Hybrid Wing Body Configuration," *48th AIAA/ASME/SAE/ASEE Joint Propulsion Conference & Exhibit*, AIAA, 2012.

[30] Drela, M., "Power Balance in Aerodynamic Flows," *AIAA Journal*, Vol. 47, No. 7, 2009.

[31] Hall, D. K., Huang, A. C., Uranga, A., Greitzer, E. M., Drela, M., and Sato, S., "Boundary Layer Ingestion Propulsion Benefit for Transport Aircraft," *Journal of Propulsion and Power*, Vol. 33, No. 5, 2017.

[32] Hall, D. K., Lieu, M. K., and Drela, M., "Aerodynamic Performance Accounting for Ultra-Integrated Air Vehicle Configurations," *AIAA SciTech Forum*, AIAA, 2019.

[33] Ahuja, J., and Mavris, D. N., "Sensitivity of Boundary Layer Ingestion Effects to Tube and Wing Airframe Design Features," *AIAA SciTech Forum*, AIAA, 2020. https://doi.org/https://doi.org/10.2514/6.2020-1523.

[34] Ahuja, J., and Mavris, D. N., "Assessment of Propulsor On-Design and Off-Design Impacts on BLI Effects," *AIAA SciTech Forum*, AIAA, 2021.

[35] Lambe, A. B., and Martins, J. R. R. A., "A Unified Description of MDO Architectures," *9th World Congress on Structural and Multidisciplinary Optimization*, 2011.

[36] McKay, M. D., J., B. R., and J., C. W., "A Comparison of Three Methods for Selecting Values of Input Variables in the Analysis of Output from a Computer Code," *Technometrics*, Vol. 21, No. 2, 1979, p. 7.

[37] Myers, R. H., Montgomery, D. C., and Anderson-Cook, C. M., *Response Surface Methodology: Process and Product Optimization Using Designed Experiments*, Wiley Series in Probability and Statistics, John Wiley and Sons, Hoboken, NJ, 2009.

[38] Cressie, N., "The Origins of Kriging," *Mathematical Geosciences*, Vol. 22, No. 3, 1990, p. 14.

[39] Jones, D. R., Schonlau, M., and Welch, W. J., "Efficient Global Optimization of Expensive Black-Box Functions," *Journal of Global Optimization*, Vol. 13, 1998, p. 37.

[40] Lee, C. H., "Bayesian Collaborative Sampling: Adaptive Learning for Multidisciplinary Design," Thesis, 2011.

[41] Jules, K., and Lin, P., "Artificial Neural Networks Applications: From Aircraft Design Optimization to Orbiting Spacecraft On-Board Environment Monitoring," Report, NASA Glenn Research Center, 2002.

[42] Secco, N. R., and Silva de Mattos, B., "Artificial Neural Networks Applied to Airplane Design," *AIAA SciTech Forum*, AIAA, 2015.

[43] Schutte, J., "Simultaneous Multi-Design Point Approach to Gas Turbine On-Design Cycle Analysis for Aircraft Engines," Thesis, 2009.

[44] Schutte, J., Tai, J., Sands, J. S., and Mavris, D. N., "Cycle Design Exploration Using Multi-Design Point Approach," *ASME Turbo Expo 2012: Turbine Technical Conference and Exposition*, ASME, 2012. https://doi.org/10.1115/GT2012-69334.

[45] Cramer, E. J., Dennis, J. E., Frank, P. D., Lewis, M., Robert, and Shubin, G. R., "Problem Formulation for Multidisciplinary Optimization," *SIAM Journal on Optimization*, Vol. 4, No. 4, 1994, pp. 754–776.

[46] Kirby, R., Michelle, and Mavris, D. N., "The Environmental Design Space," *28th International Congress of the Aeronautical Sciences*, ICAS, 2008.

[47] McCullers, L. A., "Aircraft Configuration Optimization Including Optimized Flight Profiles," *NASA Symposium on Recent Experiences in Multidisciplinary Analysis and Optimization*, NASA, 1984.

[48] Lytle, J. K., "The Numerical Propulsion System Simulation: A Multidisciplinary Design System for Aerospace Vehicles," *14th International Symposium on Air Breathing Engines*, NASA, 1999.

[49] Tong, M. T., and Naylor, B. A., "An Object-Oriented Computer Code for Aircraft Engine Weight Estimation," Report, NASA Glenn Research Center, 2009.

[50] Boeing, "737 MAX Airplane Characteristics for Airport Planning (Rev. B)," Report, Boeing Commercial Airplanes, 2018.

[51] Hardin, L. W., Tillman, G., Sharma, O. P., Berton, J., and Arend, D. J., "Aircraft System Study of Boundary Layer Ingesting Propulsion," *48th AIAA/ASME/SAE/ASEE Joint Propulsion Conference & Exhibit*, AIAA, 2012.

[52] Derringer, G., and Suich, R., "Simultaneous Optimization of Several Response Variables," *Journal of Quality Technology*, Vol. 12, No. 4, 1980, pp. 214–219. https://doi.org/10.1080/00224065.1980.11980968, URL https://doi.org/10.1080/00224065.1980.11980968.